2018

Anisotropy and Phonon Modes from Analysis of the Dielectric Function Tensor and the Inverse Dielectric Function Tensor of Monoclinic Yttrium Orthosilicate

Alyssa Mock
University of Nebraska-Lincoln, alyssalynnmock@gmail.com

Rafal Korlacki
University of Nebraska-Lincoln, rkorlacki2@unl.edu

Sean Knight
University of Nebraska-Lincoln, seanknight@unomaha.edu

Mathias Schubert
University of Nebraska-Lincoln, schubert@engr.unl.edu

Anisotropy and phonon modes from analysis of the dielectric function tensor and the inverse dielectric function tensor of monoclinic yttrium orthosilicate

A. Mock,[1,*] R. Korlacki,[1] S. Knight,[1] and M. Schubert[1,2,3]

[1]*Department of Electrical and Computer Engineering and Center for Nanohybrid Functional Materials, University of Nebraska, Lincoln, Nebraska 68588, USA*

[2]*Leibniz Institute for Polymer Research, Dresden D-01005, Germany*

[3]*Terahertz Materials Analysis Center, Department of Physics, Chemistry, and Biology (IFM), Linköping University, SE 58183 Linköping, Sweden*

(Received 20 November 2017; published 17 April 2018)

We determine the frequency dependence of the four independent Cartesian tensor elements of the dielectric function for monoclinic symmetry Y_2SiO_5 using generalized spectroscopic ellipsometry from 40–1200 cm^{-1}. Three different crystal cuts, each perpendicular to a principle axis, are investigated. We apply our recently described augmentation of lattice anharmonicity onto the eigendielectric displacement vector summation approach [A. Mock *et al.*, Phys. Rev. B **95**, 165202 (2017)], and we present and demonstrate the application of an eigendielectric displacement loss vector summation approach with anharmonic broadening. We obtain an excellent match between all measured and model-calculated dielectric function tensor elements and all dielectric loss function tensor elements. We obtain 23 A_u and 22 B_u symmetry long-wavelength active transverse and longitudinal optical mode parameters including their eigenvector orientation within the monoclinic lattice. We perform density functional theory calculations and obtain 23 A_u symmetry and 22 B_u transverse and longitudinal optical mode parameters and their orientation within the monoclinic lattice. We compare our results from ellipsometry and density functional theory and find excellent agreement. We also determine the static and above reststrahlen spectral range dielectric tensor values and find a recently derived generalization of the Lyddane-Sachs-Teller relation for polar phonons in monoclinic symmetry materials satisfied [M. Schubert, Phys Rev. Lett. **117**, 215502 (2016)].

DOI: 10.1103/PhysRevB.97.165203

I. INTRODUCTION

The optical properties of rare-earth ion doped single crystal materials have been the focus of substantial interest over the recent past. Their unique optical properties render these materials highly suitable, for example, in optical applications as active laser media [1–6], in optical signal processing [7,8], in quantum optics [9–11], and in quantum optical information technologies [12,13]. Rare-earth Ce^{3+} or Eu^{3+} doped monoclinic yttrium orthosilicate (Y_2SiO_5) can be used as phosphorous material [14–18] or as scintillator material for detection of x rays and γ rays [19]. Pr^{3+}-doped Y_2SiO_5 was investigated for electromagnetically induced transparency [20]. Cr^{4+}-doped Y_2SiO_5 has been studied for use as a saturable absorber in Q-switching laser devices [21,22].

Despite its wide use in visible spectral range optical applications, a rather incomplete knowledge seems to exist about its accurate long-wavelength optical properties. For example, a complete set of the transverse optical (TO) and longitudinal optical (LO) phonon mode frequencies, amplitudes, and eigendielectric displacement vectors has not been determined, neither by theory nor by experiment. Infrared (IR) spectra measurements and a tentative phonon band assignment were performed by Lazarev *et al.* [23]. Raman investigations have been performed by Voron'ko *et al.* [24] and by Zheng *et al.* [25]. Fourier transform IR (FTIR) spectroscopy analysis with incomplete TO mode assignment was performed recently by Höfer *et al.* [26]. The LO mode parameters remain obscure thus far. To our best knowledge, no phonon mode calculations were performed for this material.

In this work, we provide a spectroscopic investigation of the long-wavelength anisotropic properties of Y_2SiO_5 by generalized spectroscopic ellipsometry (GSE). GSE is a convenient, contactless, nondestructive technique, which utilizes polarization of light transmitted through or reflected off an arbitrarily anisotropic sample allowing for the determination of both the real and imaginary parts of all nine complex dielectric function tensor elements. Recently, GSE has been used to characterize monoclinic materials. Jellison *et al.* first reported on the determination of the dielectric function of a monoclinic single-crystalline cadmium tungstate ($CdWO_4$ or CWO) using GSE in the spectral range of 1.5 to 4 eV and reported the need for four independent dielectric function tensor elements when describing the full spectral response of the monoclinic samples. This requirement differed from all previously GSE-investigated anisotropic materials with orthorhombic, hexagonal, and tetragonal crystal symmetries where a maximum of three independent tensor elements sufficed [27]. Jellison *et al.* also reported on the determination of the four real values of the dielectric function tensor of the monoclinic crystal lutetium oxyorthosilicate (Lu_2SiO_5 or LSO) using GSE in the spectral range of 200 to 850 nm [28].

*amock@huskers.unl.edu; http://ellipsometry.unl.edu

We have recently reported that an eigendielectric displacement vector summation (EDVS) approach can be used as a physical model approach to explain and line-shape match experimentally determined dielectric function tensor elements of materials with monoclinic and triclinic symmetries [29,30]. For long-wavelength excitations, the EDVS approach is equivalent to the microscopic Born-Huang description of polar lattice vibrations in the harmonic approximation [31]. The EDVS approach goes beyond the Born-Huang description because it provides access to the LO mode properties including their eigendielectric displacement loss directions. We applied the EDVS approach to monoclinic β-Ga_2O_3 [29,32] and $CdWO_4$ [33] and determined the complete set of long-wavelength TO and LO excitations including their directions within the monoclinic lattices. It was further shown that the EDVS approach leads to a revised formulation of the Lyddane-Sachs-Teller (LST) relation [34], derived originally for isotropic materials, for materials with monoclinic and triclinic crystal symmetries. In the generalized-LST relation, the ratio of the determinants of the anisotropic static and high-frequency dielectric permittivity tensors is related to the squares of the ratios of all LO and TO mode frequencies, respectively [30].

We have described recently the need to augment anharmonic lattice broadening effects onto the EDVS approach for correct match of measured dielectric function spectra from crystals with monoclinic symmetry. The anharmonic broadening was proposed for orthorhombic and higher symmetry materials by Berreman and Unterwald [35] and Lowndes [36] (BUL broadening). We successfully demonstrated the augmentation of the BUL broadening for $CdWO_4$ [33].

In this work, we demonstrate that the EDVS approach can be used to also describe the complete dielectric loss response tensor for monoclinic materials. Thereby, we describe the eigendielectric displacement loss vector summation (EDLVS) approach. The EDLVS approach permits direct determination of the LO mode frequencies, broadening, amplitude, and eigenpolarization direction parameters. This approach dispenses with the need of numerical root finding algorithms in order to derive the LO mode frequencies from the EDVS approach. Both approaches, EDVS and EDLVS, while using the same mathematical form, provide useful access to physical parameters of TO and LO modes directly from measured quantities. We augment the same anharmonic broadening (BUL broadening) onto the EDLVS approach, and demonstrate an excellent match between experimental and model calculated data sets for crystals of monoclinic Y_2SiO_5. Thereby, we identify and determine the full set of long-wavelength active phonon modes for Y_2SiO_5. In this paper, we discuss the results of multiple approaches, simultaneously performing best-match calculation procedures using complex-valued spectra of the determinant and the inverse determinant of the dielectric tensor, as well as the dielectric tensor element spectra and the inverse dielectric tensor element spectra.

In parallel with experimental studies, Y_2SiO_5 has been studied computationally using density functional theory (DFT). These studies were motivated by potential applications of the material, for example, in barrier coatings (and hence focused on mechanical and thermal properties, and defects [37,38]), and as a host matrix for doping with rare-earth elements [39]. To the best of our knowledge, there is no comprehensive DFT study of phonons in Y_2SiO_5 available so far. It is worth noting that Y_2SiO_5 is isostructural with a number of rare-earth silicates, from Dy_2SiO_5 to Lu_2SiO_5 [40]. Thus, Y_2SiO_5 can be a convenient model system for a range of other materials.

II. THEORY

A. Symmetry

Monoclinic Y_2SiO_5 belongs to the space group 15 (centered monoclinic). The International Tables for Crystallography [41] list 18 alternative choices of the unit cell for this space group and several of them have been used for Y_2SiO_5 in the literature. The crystallographic standard for monoclinic cells requires choosing a cell with the shortest two translations in the net perpendicular to the symmetry direction $\mathbf{b}$, with $\mathbf{c} < \mathbf{a}$, β nonacute, and appropriate centering [42,43]. In the case of Y_2SiO_5 these requirements are met by choosing the $I2/c$ cell, which we will consistently use throughout this paper. The structural parameters of the unit cell are discussed in the next section.

B. Density functional theory

Theoretical calculations of long-wavelength active Γ-point phonon frequencies were performed by plane-wave DFT using Quantum ESPRESSO (QE) [48]. We used the exchange correlation functional of Perdew and Zunger (PZ) [49]. We employ optimized norm-conserving Vanderbilt (ONCV) scalar-relativistic pseudopotentials [50], which we generated for the PZ functional using the code ONCVPSP [51] with the optimized parameters of the SG15 distribution of pseudopotentials [52]. The initial parameters of the unit cell and atomic positions were taken from Ref. [45]. The calculations were performed in a primitive cell $\mathbf{p}_1 = \mathbf{a}$, $\mathbf{p}_2 = \mathbf{b}$, $\mathbf{p}_3 = (\mathbf{a} + \mathbf{b} + \mathbf{c})/2$ appropriate for the body-centered $I2/c$ cell. The conversions between equivalent cells and the preparation of the primitive cell were performed with the help of VESTA [53] and CIF2CELL [54]. The initial structure was first relaxed to force levels less than 10^{-4} Ry bohr^{-1}. A regular shifted $4 \times 4 \times 4$ Monkhorst-Pack grid was used for sampling of the Brillouin zone [55]. A convergence threshold of 1×10^{-12} Ry was used to reach self-consistency with a large electronic wave function cutoff of 100 Ry. The comparison of resulting optimized cell parameters with the existing literature data are listed in Tables I (unit cell parameters) and II (atomic positions). The relaxed cell was used for subsequent phonon calculations, which are described in Sec. IV A.

C. TO and LO mode frequencies and vectors

Two characteristic sets of eigenmodes can be defined from the frequency-dependent dielectric function tensor, $\varepsilon(\omega)$, and dielectric loss function tensor, $\varepsilon^{-1}(\omega)$. These belong to the TO and LO modes. TO modes occur at frequencies in which dielectric resonance occurs for electric fields along $\hat{\mathbf{e}}_l$ with eigendielectric displacement unit vectors then defined as $\hat{\mathbf{e}}_l = \hat{\mathbf{e}}_{\mathrm{TO},l}$. Similarly, LO modes occur when the dielectric loss approaches infinity for electric fields along $\hat{\mathbf{e}}_l$ with eigendielectric displacement unit vectors then defined as $\hat{\mathbf{e}}_l = \hat{\mathbf{e}}_{\mathrm{LO},l}$. This can

TABLE I. Comparison between the experimental and theoretical lattice constants (in Å; monoclinic angle β in °).

	Exp.[a]	Exp.[b]	Exp.[c]	Exp.[d]	Calc.[e]	Calc.[f]	Calc.[g]
a	12.38	12.64	12.490	12.469	12.402	12.33	12.847
b	6.689	6.82	6.721	6.710	6.6149	6.594	6.807
c	10.34	10.52	10.410	10.388	10.237	10.23	10.722
β	102.53	102.50	102.65	102.68	101.98	102.2	107.15

[a]Ref. [44].
[b]Ref. [45].
[c]Ref. [46].
[d]Ref. [47], Cr doped.
[e]This work, LDA-PZ.
[f]Refs. [37] and [38], LDA.
[g]Ref. [39], LDA-OLCAO.

be written as

$$|\det\{\varepsilon(\omega=\omega_{\mathrm{TO},l})\}|\rightarrow\infty, \tag{1a}$$

$$|\det\{\varepsilon^{-1}(\omega=\omega_{\mathrm{LO},l})\}|\rightarrow\infty, \tag{1b}$$

$$\varepsilon^{-1}(\omega=\omega_{\mathrm{TO},l})\hat{\mathbf{e}}_{\mathrm{TO},l}=0, \tag{1c}$$

$$\varepsilon(\omega=\omega_{\mathrm{LO},l})\hat{\mathbf{e}}_{\mathrm{LO},l}=0, \tag{1d}$$

TABLE II. Calculated equilibrium structural parameters of Y_2SiO_5 determined in this work in comparison with selected literature values. Atomic positions are given in fractional coordinates of **a**, **b**, and **c**, respectively. For the sake of consistency literature data from different sources have been converted to the same equivalent $I2/c$ cell and atomic positions, and are provided at the same level of accuracy.

	Exp. (Ref. [45])		
Y1	0.463	0.241	0.432
Y2	0.143	−0.380	0.308
Si	−0.316	0.414	0.380
O1	0.126	0.287	0.292
O2	0.407	0.492	0.063
O3	0.204	0.372	0.029
O4	0.188	0.094	−0.216
O5	0.019	0.415	−0.375
	Exp. (Ref. [46])		
Y1	0.463	0.243	0.429
Y2	0.141	−0.378	0.306
Si	−0.319	0.407	0.373
O1	0.118	0.287	0.300
O2	0.411	0.498	0.054
O3	0.202	0.343	0.032
O4	0.203	0.071	−0.237
O5	0.015	0.398	−0.382
	Calc. (this work)		
Y1	0.464	0.244	0.426
Y2	0.139	−0.368	0.307
Si	−0.318	0.408	0.371
O1	0.117	0.293	0.300
O2	0.413	0.508	0.058
O3	0.202	0.353	0.029
O4	0.201	0.063	−0.246
O5	0.019	0.403	−0.381

where l is an index for multiple frequencies in the sets [30].

1. The eigendielectric displacement approach

$\varepsilon(\omega)$. The EDVS approach can be used to best-match model calculate the dielectric function tensor of materials with monoclinic symmetry [29,30,33]. The dielectric function tensor ε is obtained from a sum of all contributions from individual dielectric resonances with displacement parallel to $\hat{\mathbf{e}}_{\mathrm{TO},l}$, added to a high-frequency scalar tensor ε_∞. The latter accounts for all eigendielectric contributions from much shorter wavelengths,

$$\varepsilon=\varepsilon_\infty+\sum_{l=1}^{N}\varrho_{\mathrm{TO},l}(\hat{\mathbf{e}}_{\mathrm{TO},l}\otimes\hat{\mathbf{e}}_{\mathrm{TO},l}), \tag{2}$$

where $\otimes$ is the dyadic product and $\varrho_{\mathrm{TO},l}$ are wavelength-dependent functions that describe the responses of the $l=1,\ldots,N$ long-wavelength active TO displacement modes. In this approach, parameters in functions $\varrho_{\mathrm{TO},l}$ and directions $\hat{\mathbf{e}}_{\mathrm{TO},l}$ are directly accessible.

$\varepsilon^{-1}(\omega)$. The EDLVS approach can be used to best-match model calculate the inverse dielectric function tensor of materials with monoclinic symmetry. The inverse dielectric function tensor ε^{-1} is obtained from a sum of all contributions from individual dielectric loss resonances with displacement parallel to $\hat{\mathbf{e}}_{\mathrm{LO},l}$, added to a high-frequency scalar tensor ε_∞^{-1}. The latter accounts for all eigendielectric loss contributions from much shorter wavelengths,

$$\varepsilon^{-1}=\varepsilon_\infty^{-1}+\sum_{l=1}^{N}\varrho_{\mathrm{LO},l}(\hat{\mathbf{e}}_{\mathrm{LO},l}\otimes\hat{\mathbf{e}}_{\mathrm{LO},l}), \tag{3}$$

where $\otimes$ is the dyadic product and $\varrho_{\mathrm{TO},l}$ are wavelength-dependent functions that describe the responses of the $l=1,\ldots,N$ long-wavelength active LO displacement loss modes. In this approach, parameters in functions $\varrho_{\mathrm{LO},l}$ and directions $\hat{\mathbf{e}}_{\mathrm{LO},l}$ are directly accessible. Without providing further proof, we state that the number of modes N in Eqs. (2) and (3) must always equal.

2. Model response functions

We use anharmonic broadened Lorentzian oscillator functions to describe the TO and LO mode responses in Eqs. (2) and Eqs. (3), respectively:

$$\varrho_{k,l}(\omega)=\frac{A_{k,l}^2-i\Gamma_{k,l}\omega}{\omega_{k,l}^2-\omega^2-i\omega\gamma_{k,l}}. \tag{4}$$

Here, $A_{k,l}$, $\omega_{k,l}$, $\gamma_{k,l}$, and $\Gamma_{k,l}$ denote the amplitude, resonance frequency, harmonic broadening, and anharmonic broadening parameters for TO ($k=$ "TO") or LO ($k=$ "LO") mode l, respectively, and ω is the frequency of the driving electromagnetic field.

3. Coordinate-invariant generalized dielectric function with anharmonic broadening

A factorized form of the dielectric function for long-wavelength active phonon modes was described by Berreman and Unterwald [35] and by Lowndes [36] which allowed for determination of TO and LO mode frequencies in materials with

multiple phonon modes. However, the Berreman-Unterwald-Lowndes (BUL) form was described under the assumption that all phonon modes which contributed to a dielectric function or inverse dielectric function under consideration must be polarized in the same crystal direction. Recently, a generalized coordinate-invariant approach was described by Schubert [30] which discussed how the determinant of the dielectric function tensor could be utilized regardless of crystal symmetry:

$$\det\{\varepsilon(\omega)\} = \det\{\varepsilon_\infty\} \prod_{l=1}^{N} \frac{\omega_{\mathrm{LO},l}^2 - \omega^2}{\omega_{\mathrm{TO},l}^2 - \omega^2}. \tag{5}$$

This approach has recently been used by us for the analysis of monoclinic β-Ga_2O_3 and $CdWO_4$ [29,33]. Note that the coordinate-invariant generalized dielectric function can reveal negative imaginary parts within distinct frequency intervals when the so-called "TO-LO" rule is broken in materials with monoclinic symmetry. We will discuss such occurrences in Sec. IV D 3.

Equation (4) can be shown to directly transform into a BUL factorized form of the dielectric function equivalent to the four-parameter semiquantum (FPSQ) model suggested by Gervais and Periou. The FPSQ model identifies $\gamma_{\mathrm{LO},l}$ to account for lifetime broadenings of LO modes different from those of associated TO modes, $\gamma_{\mathrm{TO},l}$ [56]. This four-parameter model has been used for accurate description of the effects of anharmonic phonon mode coupling in anisotropic materials [56–59].

This inclusion of anharmonic broadening into the generalized coordinate-invariant generalized dielectric function modifies Eq. (5) into the form

$$\det\{\varepsilon(\omega)\} = \det\{\varepsilon_\infty\} \prod_{l=1}^{N} \frac{\omega_{\mathrm{LO},l}^2 - \omega^2 - i\omega\gamma_{\mathrm{LO},l}}{\omega_{\mathrm{TO},l}^2 - \omega^2 - i\omega\gamma_{\mathrm{TO},l}}. \tag{6}$$

4. Coordinate-invariant generalized dielectric loss function with anharmonic broadening

A function analogous to Eq. (6) can be obtained for the dielectric loss response and has the following form:

$$\det\{\varepsilon^{-1}(\omega)\} = \det\left\{\varepsilon_\infty^{-1}\right\} \prod_{l=1}^{N} \frac{\omega_{\mathrm{TO},l}^2 - \omega^2 - i\omega\gamma_{\mathrm{TO},l}}{\omega_{\mathrm{LO},l}^2 - \omega^2 - i\omega\gamma_{\mathrm{LO},l}}. \tag{7}$$

5. Coordinate system for Y_2SiO_5

For monoclinic Y_2SiO_5 we utilize the orthorhombic system $D_1 \times D_2 \times \mathbf{b}$. Mutually perpendicular D_1 and D_2 lie within the **a**-**c** plane. In Fig. 1 the orthorhombic system $D_1 \times D_2 \times \mathbf{b}$ is shown together with the choice of our sample coordinate system (x, y, z), with x parallel to $-D_2$, y parallel to $-D_1$, and z parallel to **b**. Note that the laboratory coordinate axes $\hat{x}$, $\hat{y}$, and $\hat{z}$ are associated with the ellipsometer system (not shown in Fig. 1), where a given sample surface is parallel to plane $\hat{x}$-$\hat{y}$ and at $\hat{z} = 0$, the plane of incidence is parallel $\hat{x}$.

6. Dielectric function tensor model for Y_2SiO_5

23 TO modes with A_u symmetry are polarized along vector **b**. 22 TO modes with B_u symmetry are polarized within the **a**-**c** plane. The dielectric tensor elements for Y_2SiO_5 are then

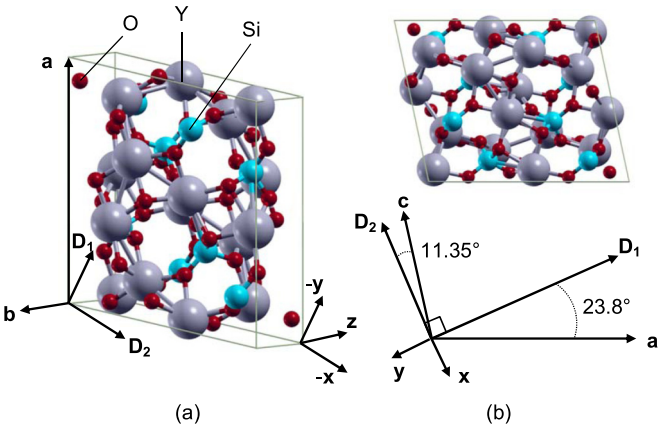

FIG. 1. (a) Unit cell of Y_2SiO_5, crystallographic vectors (**a**, **b**, **c**), principal directions of the biaxial optical indicatrix (D_1, D_2, D_3) as defined in Ref. [1] (D_3 is collinear with **b**), and sample Cartesian coordinate system (x, y, z) used in this work. (b) View onto the **a**-**c** plane along vector **b**, which points into the plane. The sample Cartesian coordinate system (x, y, z) aligns with $-D_2$, $-D_1$, and **b** as shown. The laboratory Cartesian coordinate system ($\hat{x}$, $\hat{y}$, $\hat{z}$) is associated with the ellipsometer instrument (not shown), where a given sample surface is parallel to plane $\hat{x}$-$\hat{y}$ and at $\hat{z} = 0$, the plane of incidence is parallel $\hat{x}$.

rendered as

$$\varepsilon_{xx} = \varepsilon_{\infty,xx} + \sum_{l=1}^{22} \varrho_{\mathrm{TO},l}^{B_u} \cos^2 \alpha_{\mathrm{TO},l}, \tag{8a}$$

$$\varepsilon_{xy} = \varepsilon_{\infty,xy} + \sum_{l=1}^{22} \varrho_{\mathrm{TO},l}^{B_u} \sin \alpha_{\mathrm{TO},l} \cos \alpha_{\mathrm{TO},l}, \tag{8b}$$

$$\varepsilon_{yy} = \varepsilon_{\infty,yy} + \sum_{l=1}^{22} \varrho_{\mathrm{TO},l}^{B_u} \sin^2 \alpha_{\mathrm{TO},l}, \tag{8c}$$

$$\varepsilon_{zz} = \varepsilon_{\infty,zz} + \sum_{l=1}^{23} \varrho_{\mathrm{TO},l}^{A_u}, \tag{8d}$$

$$\varepsilon_{xy} = \varepsilon_{yx}, \tag{8e}$$

$$\varepsilon_{xz} = \varepsilon_{zx} = \varepsilon_{zy} = \varepsilon_{yz} = 0, \tag{8f}$$

where angle $\alpha_{\mathrm{TO},l}$ denotes the orientation of the TO eigendielectric displacement vectors with B_u symmetry relative to crystal vector **a**.

7. Dielectric loss function tensor model for Y_2SiO_5

23 LO modes with A_u symmetry are polarized along the vector **b**. 22 LO modes with B_u symmetry are polarized within the **a**-**c** plane. The dielectric loss tensor elements for Y_2SiO_5 are then rendered as

$$\varepsilon_{xx}^{-1} = \varepsilon_{\infty,xx}^{-1} + \sum_{l=1}^{22} \varrho_{\mathrm{LO},l}^{B_u} \cos^2 \alpha_{\mathrm{LO},l}, \tag{9a}$$

$$\varepsilon_{xy}^{-1} = \varepsilon_{\infty,xy}^{-1} + \sum_{l=1}^{22} \varrho_{\mathrm{LO},l}^{B_u} \sin \alpha_{\mathrm{LO},l} \cos \alpha_{\mathrm{LO},l}, \tag{9b}$$

TABLE III. DFT results for phonon modes with B_u symmetry in units of reciprocal centimeters (cm^{-1}), debyes (D), angstroms (Å), angular degrees (°), and atomic mass units (amu). Angles are given with respect to the crystallographic direction **a**.

Mode	$\omega_{TO,l}$ (cm^{-1})	$A^2_{TO,l}$ [(D/Å)^2/amu]	$\alpha_{TO,l}$ (°)	$\omega_{LO,l}$ (cm^{-1})	$A^2_{LO,l}$ [(D/Å)^2/amu]	$\alpha_{LO,l}$ (°)
1	966.11	84.81	29.47	1045.30	132.5	27.6
2	891.27	32.54	135.54	951.88	118.4	120.3
3	856.41	44.44	116.15	875.34	7.638	97.8
4	853.56	1.90	105.12	853.72	0.0524	49.2
5	558.53	32.50	49.40	631.63	65.78	51.9
6	527.01	10.12	126.41	558.53	32.41	139.3
7	502.50	39.43	43.20	527.01	10.12	36.4
8	493.58	3.30	104.31	501.33	7.343	132.9
9	446.32	14.93	108.07	478.09	13.51	133.5
10	406.86	4.07	61.75	425.91	10.34	160.2
11	380.05	24.87	156.16	406.86	4.071	151.4
12	323.99	38.31	100.56	364.45	6.495	83.0
13	309.05	25.65	175.48	323.99	38.29	10.5
14	303.80	2.43	67.12	304.92	0.0905	76.3
15	268.70	4.92	69.25	274.71	0.8969	83.8
16	244.06	31.34	131.25	268.36	1.739	158.5
17	233.69	12.55	13.39	244.06	31.19	41.2
18	219.59	8.19	30.63	224.05	0.1918	44.7
19	166.79	1.15	107.14	168.38	0.1233	96.5
20	150.81	2.24	79.28	153.95	0.1943	73.4
21	108.39	0.85	145.34	110.01	0.0722	148.1
22	43.66	0.98	71.93	49.12	0.1266	67.2

$$\varepsilon_{yy}^{-1} = \varepsilon_{\infty,yy}^{-1} + \sum_{l=1}^{22} \varrho_{LO,l}^{B_u} \sin^2 \alpha_{LO,l}, \tag{9c}$$

$$\varepsilon_{zz}^{-1} = \varepsilon_{\infty,zz}^{-1} + \sum_{l=1}^{23} \varrho_{LO,l}^{A_u}, \tag{9d}$$

$$\varepsilon_{xy}^{-1} = \varepsilon_{yx}^{-1}, \tag{9e}$$

$$\varepsilon_{xz}^{-1} = \varepsilon_{zx}^{-1} = \varepsilon_{zy}^{-1} = \varepsilon_{yz}^{-1} = 0, \tag{9f}$$

where angle $\alpha_{LO,l}$ denotes the orientation of the TO eigendielectric displacement vectors with B_u symmetry relative to crystal vector **a**.

8. Complementary parameter analyses

Equations (8) and (9), augmented with response functions in Eq. (4), are fully complementary, and one set of parameters (ε_∞, $A_{TO,l}$ $\omega_{TO,l}$, $\gamma_{TO,l}$, $\Gamma_{TO,l}$, $\hat{\mathbf{e}}_{TO,l}$) is in principle sufficient to determine the other set of parameters (ε_∞^{-1}, $A_{LO,l}$ $\omega_{LO,l}$, $\gamma_{LO,l}$, $\Gamma_{LO,l}$, $\hat{\mathbf{e}}_{LO,l}$). Analysis of experimental dielectric function data using Eq. (8) directly permits access to TO mode parameters, including their orientations. Analysis of experimental dielectric loss function data using Eqs. (9) directly permits access to LO mode parameters, including their orientations. The immediate advantage of having wavelength-by-wavelength determined data for a dielectric function tensor available is to also have its inverse then available. The dielectric (loss) tensor elements reveal peak maxima in the imaginary parts that are directly associated with TO (LO) modes. Hence, one can read by "eye inspection" already from raw data where to anticipate TO and LO mode parameters.

Mayerhöfer *et al.* determined LO mode frequencies from modeling reflectance data of anisotropic materials parametrizing the dielectric function tensor using its inverse and the LO mode parameter set [60]. We have previously shown that LO mode frequencies in monoclinic materials can be determined by simply observing maxima in the inverse dielectric tensor [29]. We have also shown that including this inverse tensor into the model analysis yields improved sensitivity to anharmonic broadening parameters [33]. In this work, we use both approaches and determine both sets of parameters, simultaneously analyzing dielectric function tensor and inverse dielectric function data.

TABLE IV. Same as Table III for A_u symmetry.

Mode	$\omega_{TO,l}$ (cm^{-1})	$A^2_{TO,l}$ [(D/Å)^2/amu]	$\omega_{LO,l}$ (cm^{-1})	$A^2_{LO,l}$ [(D/Å)^2/amu]
1	956.65	1.80	977.36	2.11
2	904.34	48.11	952.03	0.81
3	872.12	25.36	881.09	0.39
4	864.40	1.38	864.66	0.05
5	589.15	12.84	615.54	1.14
6	546.78	6.14	555.53	0.51
7	526.02	0.06	526.11	0.06
8	499.19	0.80	501.68	0.38
9	426.55	13.91	473.15	1.08
10	418.49	0.58	418.86	0.06
11	379.78	0.73	400.33	0.53
12	354.79	26.59	379.03	0.09
13	339.33	14.90	344.73	0.11
14	315.95	5.49	319.40	0.12
15	274.18	1.90	279.51	0.25
16	250.40	14.03	266.87	0.23
17	229.70	2.77	233.56	0.12
18	218.35	10.43	224.89	0.10
19	208.79	0.02	208.81	0.01
20	182.75	8.59	190.28	0.13
21	154.73	1.14	155.86	0.05
22	112.79	0.45	113.64	0.04
23	104.07	0.49	104.91	0.04

D. Generalized ellipsometry

Generalized ellipsometry has been successfully used previously to investigate anisotropic materials including biaxial, uniaxial, and multilayered materials as well as metamaterials [57–59,61–77]. Recently, it has been applied to monoclinic materials as well [29,30,32,33,78–81]. Following the same approach used previously for β-Ga_2O_3 [29,32] and $CdWO_4$ [33], data from multiple samples, multiple azimuths, and multiple angles of incidence are investigated and analyzed simultaneously for Y_2SiO_5.

1. Mueller matrix formalization

In generalized ellipsometry, the Mueller matrix can be used to describe interaction of electromagnetic plane waves with anisotropic samples. Real-valued 4×4 Mueller matrix

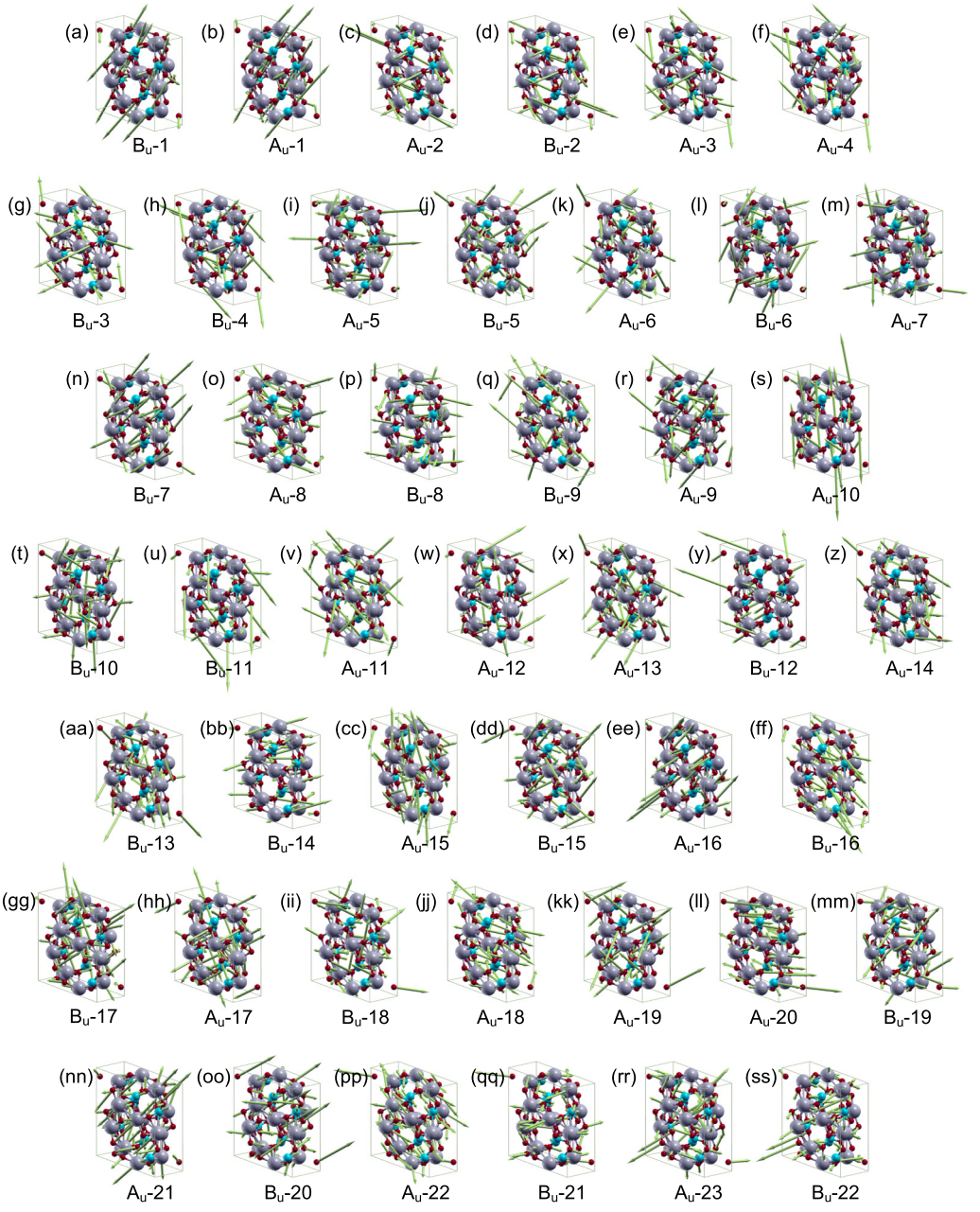

FIG. 2. Renderings of TO phonon modes in Y_2SiO_5 with A_u and B_u symmetry as labeled for each mode and presented in the order of decreasing frequency (wave number). The phonon mode parameters calculated using DFT are presented in Tables III and IV.

elements are obtained which connect the Stokes vector components before and after interaction with the sample,

$$\begin{pmatrix} S_0 \\ S_1 \\ S_2 \\ S_3 \end{pmatrix}_{\text{output}} = \begin{pmatrix} M_{11} & M_{12} & M_{13} & M_{14} \\ M_{21} & M_{22} & M_{23} & M_{24} \\ M_{31} & M_{32} & M_{33} & M_{34} \\ M_{41} & M_{42} & M_{43} & M_{44} \end{pmatrix} \begin{pmatrix} S_0 \\ S_1 \\ S_2 \\ S_3 \end{pmatrix}_{\text{input}}, \tag{10}$$

with the Stokes vector components defined by $S_0 = I_p + I_s$, $S_1 = I_p - I_s$, $S_2 = I_{45} - I_{-45}$, $S_3 = I_{\sigma+} - I_{\sigma-}$. Here, I_p, I_s, I_{45}, I_{-45}, $I_{\sigma+}$, and $I_{\sigma-}$ denote the intensities for the p-, s-, $+45^\circ$, -45°, right-handed, and left-handed circularly polarized light components, respectively [82].

2. *Wavelength-by-wavelength analysis*

In order to extract physical parameters, data must be analyzed through a best-match model calculation procedure. We apply a half-infinite, two-phase model to Y_2SiO_5 where two half-infinite media, ambient (air) and monoclinic Y_2SiO_5, are separated by the planar surface of the crystal [82–86]. In this approach, the Euler angles describing the orientation of the crystal axes and the elements of the monoclinic dielectric tensor are considered free parameters. The dielectric function tensor elements are expressed as wavelength-dependent model functions, thereby allowing for determination of the tensor elements in the so-called wavelength-by-wavelength model analysis approach.

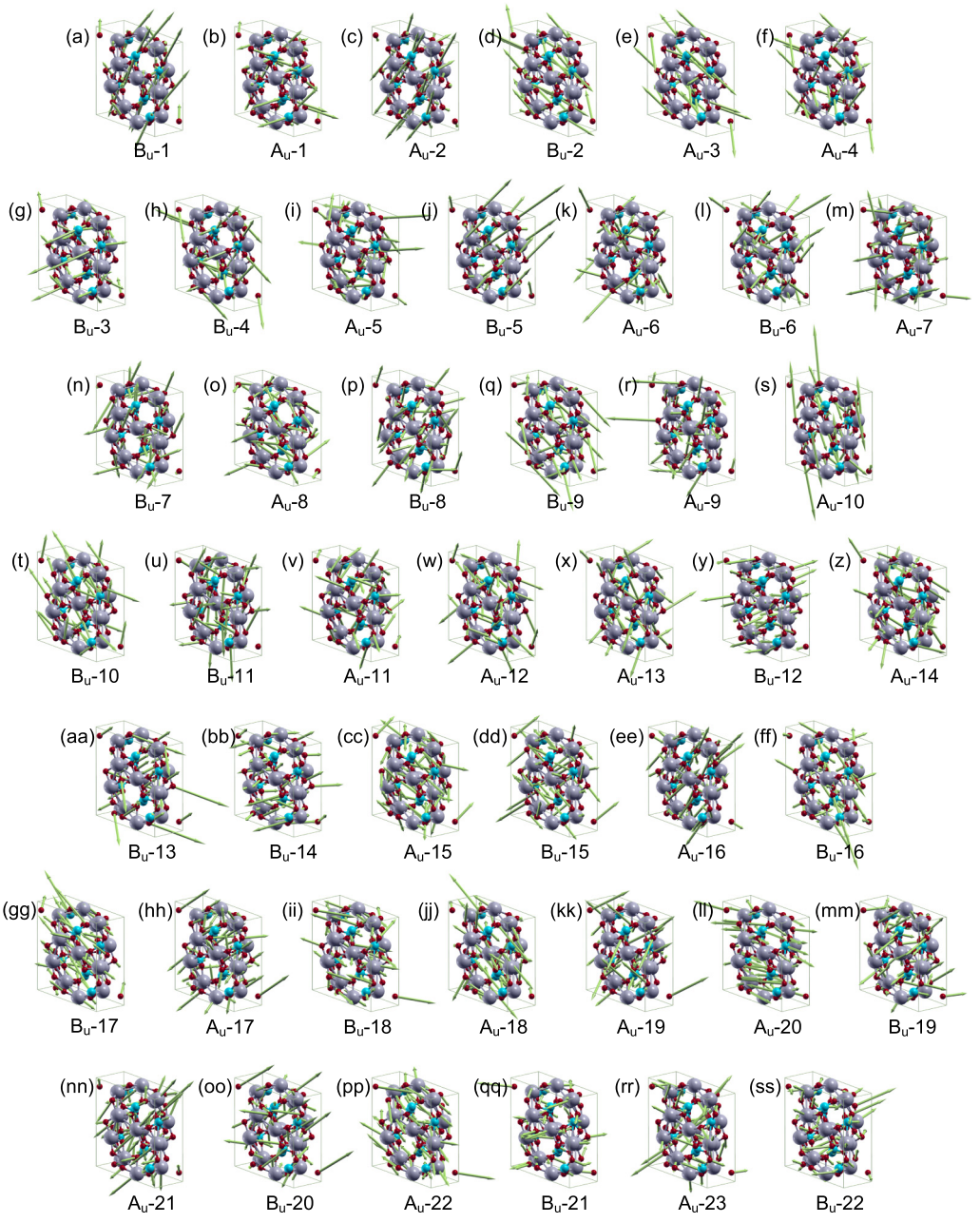

FIG. 3. Renderings of LO phonon modes in Y_2SiO_5 with A_u and B_u symmetry as labeled for each mode and presented in the same order as TO modes in Fig. 2. The phonon mode parameters calculated using DFT are presented in Tables III and IV.

We establish two Cartesian coordinate systems such that our sample coordinate system may be related to the crystallographic axes or the so-called principle directions of the biaxial optical indicatrix of Y_2SiO_5 [87]. The laboratory coordinate system is determined by the ellipsometer instrument and is defined by the sample holder and plane of incidence. The sample surface is defined as the $\hat{x}$-$\hat{y}$ plane, the plane of incidence is parallel to $\hat{x}$, and the sample normal defines the $\hat{z}$ axis which points into the sample. We assign the sample system (x, y, z) to coincide with the axes of the optical indicatrix (D_1, D_2, D_3), as defined in Ref. [1]. Note that D_3 coincides with $-\mathbf{b}$ (Fig. 1), where we follow the notation given in Ref. [1]. Due to the monoclinic symmetry the dielectric tensor ε for Y_2SiO_5 contains shear elements and with the choice of coordinates above can now be expressed as

$$\boldsymbol{\varepsilon} = \begin{pmatrix} \varepsilon_{xx} & \varepsilon_{xy} & 0 \\ \varepsilon_{xy} & \varepsilon_{yy} & 0 \\ 0 & 0 & \varepsilon_{zz} \end{pmatrix}. \tag{11}$$

An Euler angle rotation can be applied to ε in order to describe the crystallographic surface and azimuthal orientation of the sample. The sample azimuth, φ, defined by an in-plane rotation with respect to sample normal, describes the mathematical rotation of a model dielectric function tensor of calculated data when compared with measured data taken at different azimuthal orientations.

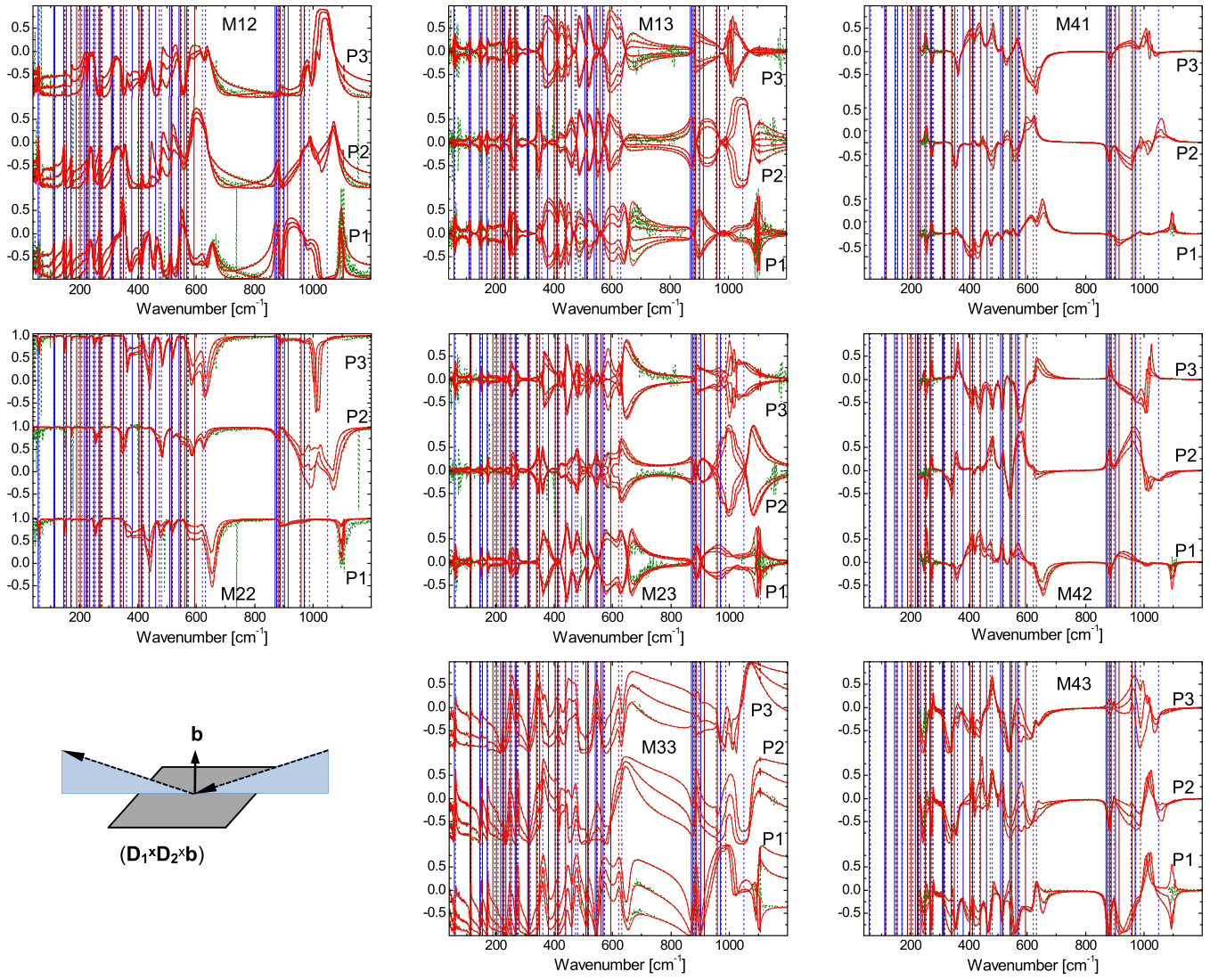

FIG. 4. Experimental (dotted, green lines) and best-match model calculated (solid, red lines) normalized Mueller matrix data obtained from a ($D_1 \times D_2 \times \mathbf{b}$) surface at three representative sample azimuth orientations [P1: $\varphi = 3.6(3)^\circ$, P2: $\varphi = 48.6(3)^\circ$, P3: $\varphi = 93.6(3)^\circ$]. Data were taken at three angles of incidence ($\Phi_a = 50^\circ, 60^\circ, 70^\circ$). Equal Mueller matrix data, symmetric in their indices, are plotted within the same panels for convenience. Vertical lines indicate positions of TO (solid lines) and LO (dotted lines) modes with B_u symmetry (blue) and A_u symmetry (brown). Due to a lack of compensator in the FIR spectral region, fourth-row elements are only available from the IR instrument limited to approximately 230 cm^{-1} and are plotted in the symmetric tensor panel locations, i.e., as the fourth column, for convenience. Note that all elements are normalized to M_{11}. The remaining Euler angle parameters are $\theta = 0.2(4)$ and $\psi = -0.1(5)$ consistent with the crystallographic orientation of the ($D_1 \times D_2 \times \mathbf{b}$) surface. The inset depicts schematically the sample surface, the plane of incidence, and the orientation of direction **b** in P1.

In a wavelength-by-wavelength approach, calculated Mueller matrix data are compared to experimentally measured Mueller matrix data. Wavelength-dependent dielectric function tensor elements ε_{xx}, ε_{yy}, ε_{xy}, and ε_{zz} are varied in order to minimize the mean-squared error (ξ) function [57,58,85,88,89]. Analysis of all samples, azimuthal orientations, and angles of incidence is performed simultaneously for all independent wavelengths yielding a single set of complex-valued, wavelength-dependent ε_{xx}, ε_{yy}, ε_{xy}, and ε_{zz} (polyfit). During the polyfit, an independent set of Euler angle parameters for each sample is utilized to describe the orientation of the principle directions and crystallographic axes at the first azimuthal position acquired.

3. Model analysis procedure

In order to reduce correlation and improve sensitivity to model parameters, multiple data sets are fitted simultaneously with multiple models. The model process is detailed below for the **a**-**c** plane with three parts. The model procedure is repeated independently for modes along **b**.

Model 1. Equations (6) and (7) are used to best-match model calculate the wavelength-by-wavelength determined determinants of ε and ε^{-1}, respectively, finding parameters $\omega_{TO,l}$, $\gamma_{TO,l}$, $\omega_{LO,l}$, $\gamma_{LO,l}$, and ε_∞. The best-match model calculated functions are represented by black solid lines in Fig. 7.

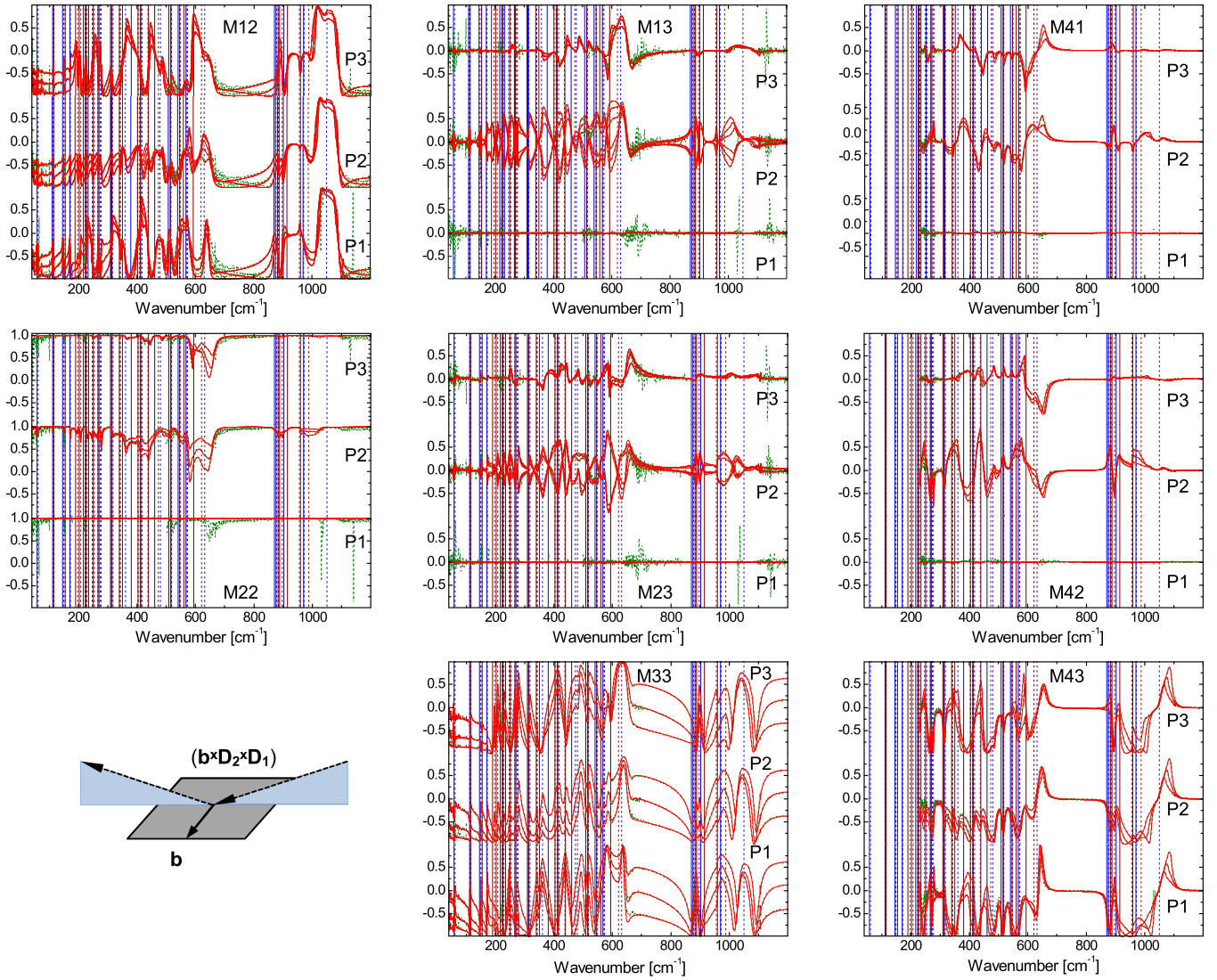

FIG. 5. Same as Fig. 4 for the ($\mathbf{b} \times D_1 \times D_2$) sample at azimuth orientation P1: $\varphi = -0.2(1)^\circ$, P2: $\varphi = 44.7(9)^\circ$, P3: $\varphi = 89.79^\circ$. $\theta = 89.(9)$ and $\psi = -1.5(7)$, consistent with the crystallographic orientation of the ($\mathbf{b} \times D_1 \times D_2$) surface. Note that in position P1, direction **b**, which is parallel to the sample surface in this crystal cut, is aligned almost perpendicular to the plane of incidence. Hence, the monoclinic plane with **a** and **c** is nearly parallel to the plane of incidence, and as a result almost no conversion of *p* to *s* polarized light occurs and vice versa. As a result, the off-diagonal block elements of the Mueller matrix are near zero. The inset depicts schematically the sample surface, the plane of incidence, and the orientation of crystal vector **b**, shown approximately for position P1.

Model 2. In addition to best-match model calculated determinants of ε and ε^{-1}, the individual wavelength-by-wavelength determined dielectric tensor elements ε_{xx}, ε_{xy}, and ε_{yy} are best-match model calculated using Eqs. (8a), (8b), and (8c), respectively, and the anharmonic Lorentzian oscillator functions in Eq. (4) to determine the additional TO mode parameters $A_{TO,l}$, $\Gamma_{TO,l}$, and $\alpha_{TO,l}$. In addition, the numerically calculated inverse of the model-calculated dielectric function tensor is matched with the wavelength-by-wavelength determined inverse of the dielectric function tensor. The best-match model calculated functions are represented by red solid lines in Figs. 6 and 8.

Model 3. In addition to best-match model calculated determinants of ε and ε^{-1}, the individual wavelength-by-wavelength determined inverse dielectric tensor elements ε_{xx}^{-1}, ε_{xy}^{-1}, and ε_{yy}^{-1} are best-match model calculated using Eqs. (9a), (9b), and (9c), respectively, and the anharmonic Lorentzian oscillator functions in Eq. (4) to determine the additional LO mode parameters $A_{LO,l}$, $\Gamma_{LO,l}$, and $\alpha_{LO,l}$. In addition, the numerically calculated inverse of the model-calculated inverse dielectric function tensor is matched with the wavelength-by-wavelength determined dielectric function tensor. The best-match model calculated functions are represented by cyan solid lines in Figs. 6 and 8.

III. EXPERIMENT

Three single-crystal samples of Y_2SiO_5 purchased from Scientific Materials Corporation were investigated. The sample dimensions were 10 mm × 10 mm × 1 mm. Investigated crystal

orientations were $D_1 \times D_2 \times \mathbf{b}$, $\mathbf{b} \times D_2 \times D_1$, and $D_1 \times \mathbf{b} \times D_2$, where primary axes D_1 and D_2 are defined in relation to the crystal vectors as described in Ref. [1] and shown in Fig. 1. All model calculations were performed using WVASE32 (J. A. Woollam Co., Inc.).

Mueller matrix data were obtained from each sample surface at five sample azimuth orientations, rotated clockwise in 45° increments. Data were taken at three angles of incidence ($\Phi_a = 50°,60°,70°$). Due to a lack of compensator in the FIR spectral region, fourth-row elements are only available from the IR instrument limited to approximately 250 cm^{-1}. All data was used for analysis but only 3 azimuthal positions for each surface are discussed and shown here. Measurements from azimuthally rotated orientations 180° apart are identical and no nonreciprocity effects were observed.

IV. RESULTS AND DISCUSSION

A. DFT phonon calculations

The phonon frequencies and transition dipole components were computed at the Γ point of the Brillouin zone using density functional perturbation theory [90]. The parameters of the TO modes were taken directly from the Γ-point calculations. The parameters of the LO modes were obtained by setting a small displacement from the Γ point. For A_u symmetry modes this displacement was in the direction of the crystal direction **b**. For the B_u modes, the entire **a**-**c** plane was probed with a fine step of 1°, and the parameters of the LO modes were taken at the direction for which the angular dependence of the mode frequency for each B_u mode had its maximum value.

The results of the phonon mode calculations for all long-wavelength active modes with B_u and A_u symmetry ($\omega_{TO,l}$, $A_{TO,l}$, $\alpha_{TO,l}$, $\omega_{LO,l}$, $A_{LO,l}$, $\alpha_{LO,l}$) are listed in Tables III and IV. Note that for modes with A_u symmetry, all eigenvectors are oriented along direction **b** and thus $\alpha_{TO,LO,l}$ are not needed. Values for $\alpha_{TO,LO,}$ for modes with B_u symmetry are counted relative to crystal direction **a** within the **a**-**c** plane. Renderings of atomic displacements for each mode were prepared using XCrysDen [91] running under Silicon Graphics Irix 6.5, and are shown in Figs. 2 and 3.

B. Mueller matrix analysis

Figures 4 and 5 show representative experimental and best-match model calculated Mueller matrix data for two of the three surfaces investigated in this work, namely the ($D_1 \times D_2 \times \mathbf{b}$) and ($\mathbf{b} \times D_1 \times D_2$) surfaces. The insets in Figs. 4 and 5 show schematically the crystal direction **b** with respect to the sample surface, and the plane of incidence is also indicated. Individual panels are shown for each Mueller matrix element and are arranged according to Mueller matrix indices. Within each panel, data from 3 different azimuthal positions (P1, P2, and P3), each 45° rotated clockwise, each with 3 angles of incidence (50°, 60°, and 70°), are presented. Data from additional positions measured are not shown for brevity.

It is observed by experiment as well as by model calculations that all Mueller matrix elements are symmetric, i.e., $M_{ij} = M_{ji}$; therefore, symmetric elements, i.e., from upper and lower diagonal parts of the Mueller matrix, are plotted within the same panels. Therefore, only panels from the upper part of a 4 × 4 matrix arrangement is presented, and because all data obtained are normalized to element M_{11}, the first column does not appear in this arrangement. Element M_{44} cannot be obtained in our current instrument configuration due to the lack of a second compensator and is therefore not presented. Data are shown for wave number range from 40 cm^{-1} to 1200 cm^{-1}, except for row $M_{4j} = M_{j4}$ which only contains data from approximately 250 cm^{-1} to 1200 cm^{-1} because the fourth row is unavailable with our FIR instrumentation. Note that the fourth-row data are plotted in the fourth column of Figs. 4 and 5 for convenience. All other panels show data obtained within the FIR range (40 cm^{-1} to 500 cm^{-1}) using our FIR instrumentation and data obtained within the IR range (500 cm^{-1} to 1200 cm^{-1}) using our IR instrumentation.

Strong anisotropy is noted in Y_2SiO_5 by the nonzero contributions in off-block diagonal elements (M_{13}, M_{23}, M_{14}, and M_{24}) and a strong dependence on azimuthal orientation is also apparent by inspection of the Mueller matrix data. Another important observation from the Mueller matrix data is that at P1 for the ($\mathbf{b} \times D_1 \times D_2$) surface in Fig. 5, where the **b** direction is parallel to the sample surface and perpendicular to the plane of incidence, the off-block diagonal elements are very nearly zero. This is because the monoclinic plane is parallel to the plane of incidence in this orientation and therefore there is no mode conversion of *s*-polarized light to *p*-polarized light and vice versa.

All data sets, while unique, share similar characteristic features at specific energies, which are indicated by vertical lines. Below, we identify these vertical lines as frequencies of all TO and LO phonon mode with A_u and B_u symmetries. Analyses of all data sets were performed simultaneously, where for each wavelength up to 792 independent data points from the multiple samples, azimuthal positions, and angles of incidence are included in the polyfit. Only 17 independent parameters are included as variables in this so-called wavelength-by-wavelength analysis, including the 8 real and imaginary parts of the dielectric tensor elements (ε_{xx}, ε_{yy}, ε_{xy}, and ε_{zz}) as well as 3 sets of wavelength-independent Euler angles to describe the sample surface and orientation. The resulting Mueller matrix rendered from this polyfit analysis is shown in Figs. 4 and 5 as red solid lines, and resulting real and imaginary parts of the dielectric tensor elements are given in Fig. 6 as green dotted lines. We find excellent agreement between our measured experimental and model-calculated Mueller matrix data, and the Euler angles determined by this analysis are consistent with the anticipated sample surfaces and crystallographic orientations. We note that the increase in noise for the dielectric function spectra towards longer wavelengths is caused by reduction of light source intensity and hence by reduction of signal level. No free charge carriers are present within the samples and the purely dielectric samples also possess very low reflectivity further reducing the signal level in the ellipsometry measurements.

C. Dielectric tensor analysis

Real and imaginary parts of the dielectric tensor elements determined by the wavelength-by-wavelength polyfit are given in Fig. 6 as green dotted lines for ε_{xx}, ε_{xy}, ε_{yy}, and ε_{zz}. One can then translate these into the inverse dielectric tensor shown as green dotted lines in Fig. 8 for ε_{xx}^{-1}, ε_{xy}^{-1}, ε_{yy}^{-1},

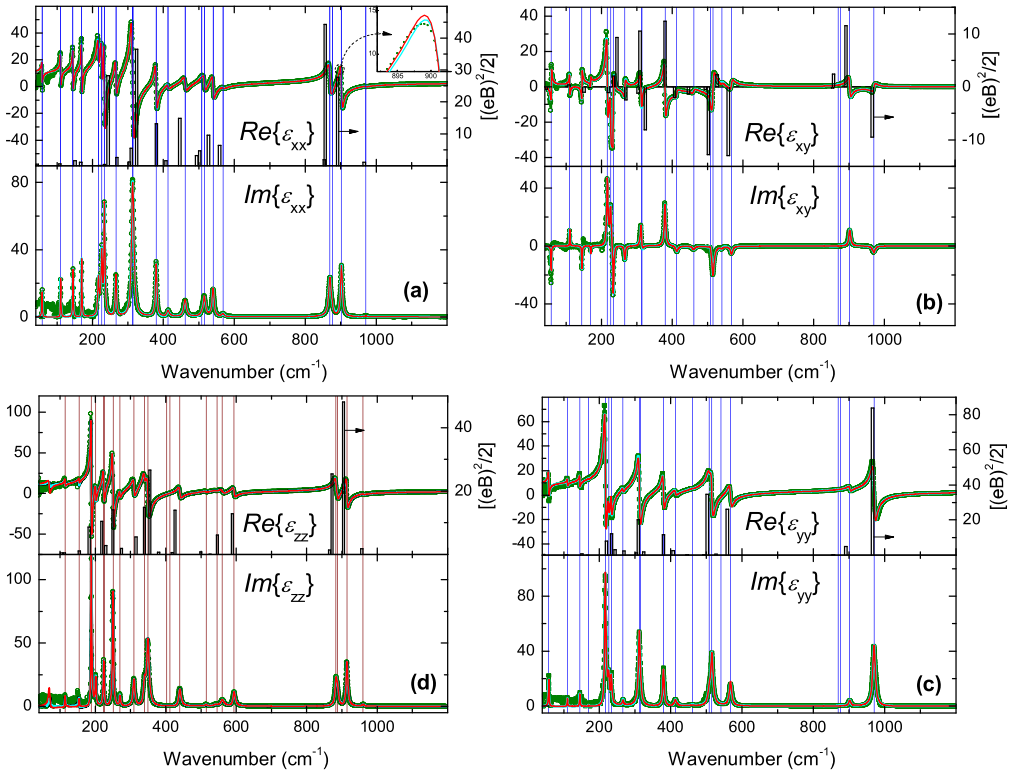

FIG. 6. Dielectric function tensor element ε_{xx} (a), ε_{xy} (b), ε_{yy} (c), and ε_{zz} (d). Green dotted lines indicate results from wavelength-by-wavelength best-match model regression analysis matching the experimental Mueller matrix data shown in Figs. 4 and 5. Solid red lines are obtained from best-match model line-shape analysis using Eqs. (8) with Eq. (4) fitted to the dielectric tensor elements. Solid cyan lines are obtained from best-match model line-shape analysis using a second set of Eqs. (8) with Eq. (4) fitted to the inverse dielectric tensor elements. Vertical lines in panel group [(a), (b), (c)] and in panel (d) indicate TO frequencies with B_u (blue) and A_u (brown) symmetry, respectively. Vertical bars indicate DFT-calculated long-wavelength transition dipole moments in atomic units projected onto axes x, y, and z as well as onto the shear plane xy.

and ε_{zz}^{-1}, and into the determinant $(\varepsilon_{xx}\varepsilon_{yy} - \varepsilon_{xy}^2)$ and inverse determinant $((\varepsilon_{xx}\varepsilon_{yy} - \varepsilon_{xy}^2)^{-1})$ as shown by green dotted lines in Fig. 7. From these, preliminary observations can be made for phonon mode properties. As we have previously reported, TO mode frequencies can be found from maxima in imaginary parts of the dielectric function tensor elements as well as the determinant [30] as shown in Figs. 6 and 7 indicated by solid vertical lines. Likewise, LO mode frequencies can be determined from maxima of the imaginary parts of the inverse dielectric function tensor and the inverse of the determinant [33] as seen in Figs. 7 and 8 indicated by dotted vertical lines. We note that panels (a), (b), and (c) in Figs. 6 and 8 share common frequencies at which maxima occur from which we identify 22 TO modes and a corresponding 22 LO modes with B_u symmetry, respectively. We also note that the imaginary part of ε_{xy} and ε_{xy}^{-1} can be positive as well as negative extrema at B_u TO and LO mode frequencies, respectively, which is due to the respective eigendielectric displacement unit vector orientation relative to direction **a**. From Eq. (8b), it is seen that the imaginary part of ε_{xy} is negative when $\alpha_{TO,l}$ is within $\{0 \ldots -\pi\}$ and positive when $\alpha_{TO,l}$ is within $\{0 \ldots \pi\}$. Therefore, for example, we observe from experiment that B_u TO modes labeled 2, 3, 4, 6, 9, 11, 12, 13, 15, 17, 18, 19, and 21 are all oriented with negative angle towards **a**.

D. Phonon mode analysis

1. *Modes with B_u symmetry in the* a-c *plane*

TO mode parameter determination. Solid red lines in Figs. 6 and 8 indicate the resulting best-match model calculations obtained from Eq. (8) using a set of anharmonically broadened Lorentzian oscillators. We find excellent agreement between our wavelength-by-wavelength and model-calculated ε and ε^{-1}. All best-match TO model parameters are summarized in Table V including amplitude ($A_{TO,l}$), frequency ($\omega_{TO,l}$), broadening ($\gamma_{TO,l}$), anharmonic broadening ($\Gamma_{TO,l}$), and eigenvector direction ($\alpha_{TO,l}$) for all TO modes ($l = 1 \ldots 22$) with B_u symmetry. Frequencies of the TO modes are indicated by solid vertical blue lines in Figs. 4, 5, 6, and 7 which align with the features observed in the data and the extrema seen in the imaginary part of the dielectric tensor.

TO mode parameters determined by Höfer *et al.* [26] are included in Table V for comparison. While we do expect 22 modes with B_u symmetry from calculations, and they do identify 22 features, it can be seen that several features determined by Höfer *et al.* do not correspond with modes determined by our analysis, specifically features identified at 974.3, 539.6, 461.5, and 231.2 cm^{-1}. In addition, several modes determined in our work are not identified by Höfer *et al.*, specifically, modes 4, 14, 21, and 22.

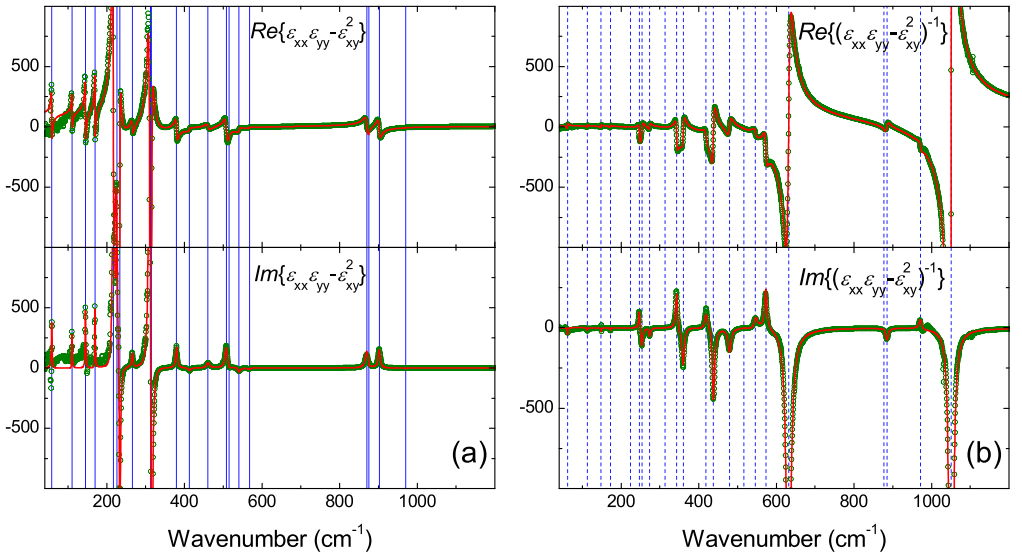

FIG. 7. (a) Real and imaginary parts of the coordinate-invariant generalized dielectric function, $\varepsilon_{xx}\varepsilon_{yy} - \varepsilon_{xy}^2$, along with its inverse (b), $(\varepsilon_{xx}\varepsilon_{yy} - \varepsilon_{xy}^2)^{-1}$. Best-match model calculated data (red, solid lines) calculated from the BUL form agree excellently with data determined from a wavelength-by-wavelength analysis. TO and LO mode parameters are determined independently of their individual polarization and amplitudes. Frequencies of TO modes are indicated with solid blue lines and frequencies of LO modes are indicated by dotted blue lines.

TO eigendielectric displacement vectors. Figure 9 displays a vector representation of the amplitude and polarization direction parameters ($A_{\mathrm{TO},l}^{B_u}$ and $\alpha_{\mathrm{TO},l}$) within the **a**-**c** plane. Results from the IR/FIR GSE model dielectric function, panel (a), are compared with long-wavelength transition dipole moments calculated from DFT, panel (b). Remarkably good agreement is

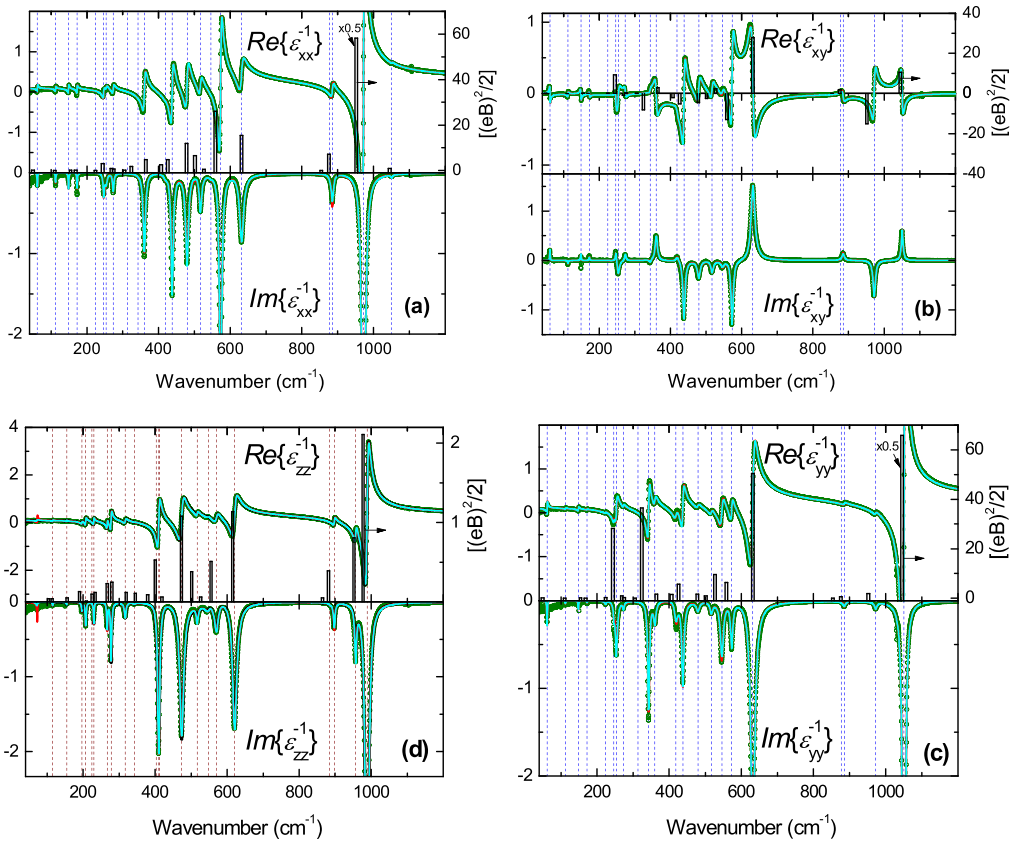

FIG. 8. Same as for Fig. 6 but for the inverse dielectric tensor. Vertical lines in panel group [(a), (b), (c)] and in panel (d) indicate LO frequencies with B_u (blue) and A_u (brown) symmetry, respectively.

TABLE V. Phonon mode parameters with B_u symmetry obtained from best-match model analysis of tensor element spectra ε and ε^{-1}, using anharmonic broadened Lorentz oscillator functions in Eq. (4) as well as by utilization of the generalized coordinate-invariant form of the dielectric function [30]. The last digit, which is determined within the 90% confidence interval, is indicated with parentheses for each parameter. Angles are given with respect to the crystallographic direction **a**. Frequencies of TO modes from Ref. [26] are included for comparison.

Mode	ω_{TO} (cm^{-1})	ω_{LO} (cm^{-1})	γ_{TO} (cm^{-1})	γ_{LO} (cm^{-1})	A_{TO} (cm^{-1})	Γ_{TO} (cm^{-1})	α_{TO} (°)	A_{LO} (cm^{-1})	Γ_{LO} (cm^{-1})	α_{LO} (°)	$\bar{\nu}_j$ (Ref. [26])
											974.3
1	970.5(9)	1050.8(0)	9.0(6)	5.8(3)	627.(2)	14.(2)	28.8(7)	251.(1)	0.3(6)	27.2(6)	970.7
2	902.1(3)	972.1(1)	6.5(1)	8.1(1)	449.(8)	−8.(0)	133.(0)	240.(5)	−0.9(2)	119.5(5)	902.5
3[a]	876.(0)	877.(0)	5.(0)	5.(2)	99.(7)	0.(0)	111.(3)	7.(4)	0.(0)	14(9)	871.0
4	869.9(0)	885.(2)	8.8(1)	7.(9)	42(0)	13.(7)	112.(7)	52.(4)	0.2(4)	92.(2)	
5	567.8(8)	631.4(9)	8.(0)	13.1(8)	294.(0)	4.(0)	40.(5)	173.(9)	−2.8(0)	52.4(1)	567.9
6	540.2(6)	573.1(2)	6.(7)	7.1(6)	246.(9)	5.(2)	108.5(7)	125.(5)	−0.8(0)	135.0(3)	540.2
											539.6
7	515.3(5)	546.(1)	8.0(4)	10.(5)	44(8)	−1(2)	52.(2)	60.(3)	0.0(8)	13.(3)	514.0
8	507.7(6)	516.6(6)	8.(1)	8.(3)	19(9)	−0.(8)	3.(4)	50.(0)	−0.3(5)	140.(9)	507.9
9	460.9(3)	479.6(7)	8.(7)	9.(6)	205.(4)	−3.(5)	100.(0)	75.(6)	0.5(3)	130.(7)	462.3
											461.5
10	412.(7)	437.8(4)	7.(9)	7.2(9)	16(1)	−(9)	6(5)	88.(2)	−0.7(6)	152.(4)	413.1
11	379.7(1)	418.(6)	5.0(9)	10.(3)	334.(6)	2.(2)	15(6)	32.(5)	−0.6(0)	47.(4)	379.5
12	314.5(8)	360.3(2)	7.(0)	7.7(0)	3(2)5	−3(0)	10(2)	58.(3)	0.2(3)	86.(9)	313.4
13	312.1(0)	343.0(6)	6.2(8)	5.(9)	37(0)	(8)	162.(7)	49.9(6)	0.0(5)	21.(2)	312.6
14	312.(2)	313.(2)	7.(3)	6.(9)	2(6)0	1(8)	72.(2)	2.7(8)	0.0(1)	23(2)	
15	266.0(1)	273.2(7)	4.1(7)	4.(7)	176.(1)	−(4)	92.(4)	19.8(1)	−0.0(6)	82.(3)	265.8
16	233.5(9)	253.6(0)	3.6(0)	6.8(2)	267.(8)	−1(4)	84.(7)	36.1(2)	−0.26(4)	178.(8)	231.3
											231.2
17	226.0(9)	246.9(3)	4.6(8)	4.3(1)	238.(7)	2(9)	14(8)	21.0(2)	−0.02(4)	78.(5)	225.4
18	216.4(7)	223.9(2)	4.5(5)	5.6(7)	339.(4)	−5(2)	177.8(1)	6.7(3)	0.03(7)	28.(7)	217.1
19	169.6(2)	172.1(8)	1.5(8)	2.1(0)	98.(9)	−4.(9)	104.(1)	8.9(5)	−0.04(9)	94.(5)	170.9
20	144.9(8)	148.4(2)	2.0(8)	2.0(1)	106.(0)	−0.(3)	83.(9)	9.4(3)	0.01(5)	78.(9)	145.0
21	110.4(2)	112.2(2)	1.5(6)	1.8(6)	70.(4)	−2.(7)	139.(3)	5.7(6)	−0.02(4)	141.(5)	
22	57.8(9)	61.7(1)	2.1(2)	1.6(9)	65.(3)	3.(9)	64.(1)	7.0(4)	0.04(8)	61.(5)	

[a]Mode parameter fit in a local region, held constant in full spectral fit procedure.

seen between the GSE and DFT resulting eigenvectors. Note that the eigenvector provides an additional mode identification mechanism. Experimentally determined modes can be compared with and sorted by calculated modes not only by frequency and amplitude, but also by orientation. Hence, in some instances here, modes observed by GSE and identified by amplitude and direction with a mode calculated by DFT may appear out of frequency sequence, that is, at slightly smaller or slightly larger frequency than predicted by DFT. Thereby, a mode may be found experimentally at a different mode index than predicted by the sequence of DFT-calculated frequencies. This occurs here for modes 3 and 4 as well as for modes 17 and 18. The experimental TO mode vector orientations agree within 25° with corresponding calculated modes with the exception of modes 8, 16, 17, and 18. Mode 8 is has the largest disagreement (GSE nearly perpendicular to DFT) which could be explained by its low amplitude and relatively large broadening. It also appears on the shoulder of a much larger nearby mode in GSE data, decreasing sensitivity to mode 8 parameters.

LO mode parameter determination. Cyan solid lines in Figs. 8 and 6 indicate the resulting best-match model calculations obtained from Eq. (8) using a second independent set of anharmonically broadened Lorentzian oscillators. We find excellent agreement between our wavelength-by-wavelength and model-calculated ε^{-1} and ε. All best-match LO model parameters are summarized in Table V including amplitude ($A_{LO,l}$), frequency ($\omega_{LO,l}$), broadening ($\gamma_{LO,l}$), anharmonic broadening ($\Gamma_{LO,l}$), and eigenvector direction ($\alpha_{LO,l}$) for all LO modes ($l = 1 \ldots 22$) with B_u symmetry. Frequencies of the LO modes are indicated by dotted vertical blue lines in Figs. 4, 5, 7, and 8 which align with the features observed in the data and the extrema seen in the imaginary part of the inverse dielectric tensor.

LO eigendielectric displacement vectors. Figure 10 displays a vector representation of the amplitude and polarization direction parameters ($A^{Bu}_{LO,k}$ and $\alpha_{LO,k}$) projected onto the **a**-**c** plane. Results from the IR/FIR GSE model dielectric function, panel (a), are compared with long-wavelength transition dipole moments calculated from DFT, panel (b). Remarkably good agreement is seen between the GSE and DFT resulting LO eigenvectors. Interestingly, while some LO mode eigenpolarization directions do not deviate very much from their TO counterparts (for example mode 1 with $\alpha_{TO,1} = 28.8°$ and $\alpha_{LO,1} = 27.2°$), most differ significantly.

2. *Modes with A_u symmetry along the crystal direction* **b**

Resulting mode parameters are described in Table VI and dielectric function and inverse dielectric function are given in Figs. 6(d) and 8(d), respectively. Red solid lines show the

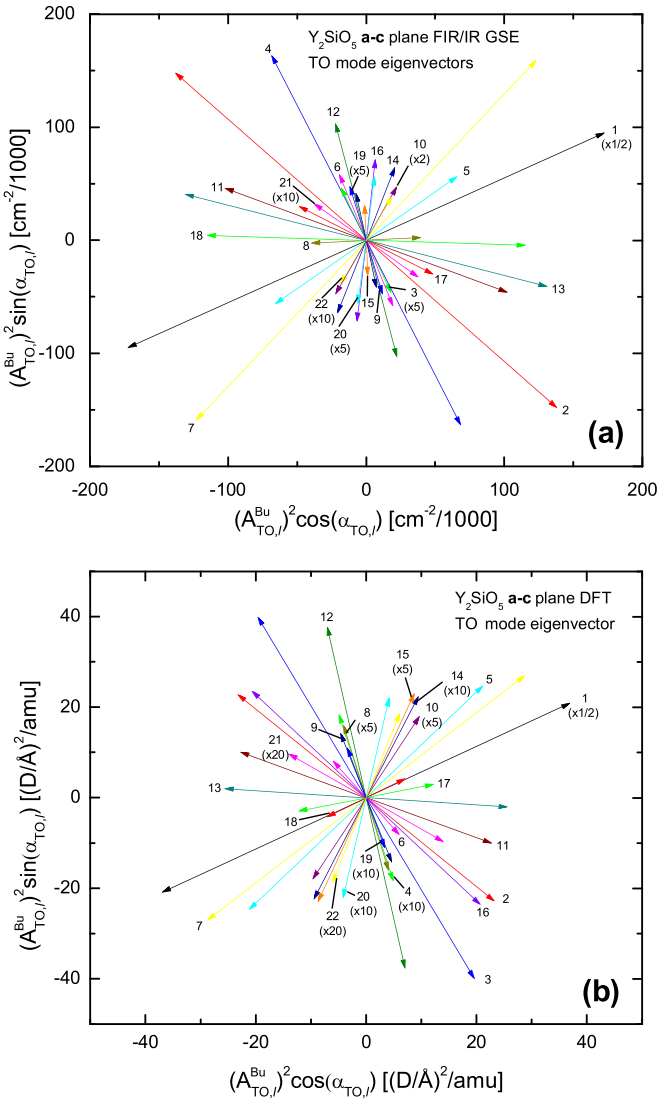

FIG. 9. (a) Schematic representation of the eigendielectric displacement vectors with GSE analysis determined amplitude $A^{B_u}_{\mathrm{TO},l}$ and orientation angle $\alpha_{\mathrm{TO},l}$ (with respect to the crystal vector **a**) of TO modes with B_u symmetry within the **a**-**c** plane. (b) DFT-calculated long-wavelength transition dipoles (intensities) of TO modes with B_u symmetry.

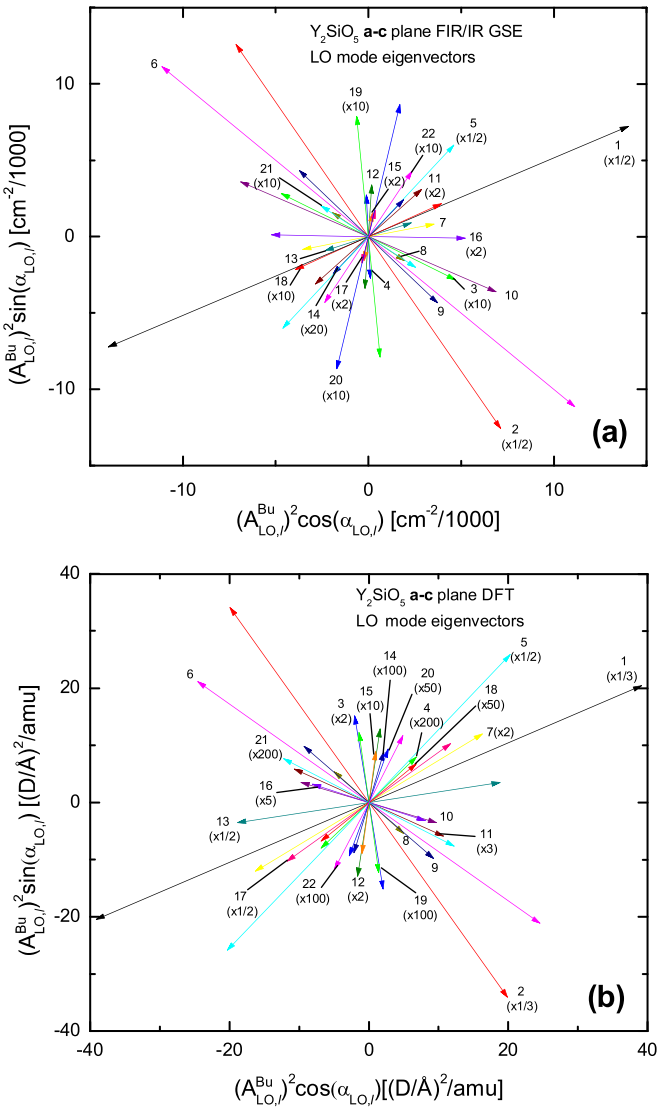

FIG. 10. (a) Schematic representation of the eigendielectric displacement loss vectors with GSE analysis determined amplitude $A^{B_u}_{\mathrm{LO},l}$ and orientation angle $\alpha_{\mathrm{LO},l}$ (with respect to the crystal vector **a**) of LO modes with B_u symmetry within the **a**-**c** plane. (b) DFT-calculated long-wavelength transition dipoles (intensities) of LO modes with B_u symmetry.

resulting model-calculated dielectric function from Eq. (8) using a set of 23 anharmonic Lorentzian oscillators [Eq. (4)] for the A_u symmetry TO modes. Similarly, the solid cyan lines indicate the resulting model-calculated dielectric function from Eq. (8) using a separate set of 23 anharmonic Lorentzian oscillators [Eq. (4)] for the A_u symmetry LO modes. Mode parameters of LO and TO frequencies and broadenings were also determined simultaneously using the BUL form Eq. (6) shown in black.

Due to many modes appearing in some narrow frequency regions, sensitivity to separate mode parameters reduces. Contributions from weak modes are easily subsumed by contributions from strong modes, necessitating several localized spectral best-match model analyses (modes 3, 4, 10, 21, and 23) and some modes required manual setting of parameters (modes 12, 21, and 23). Frequencies of TO modes with A_u symmetry are indicated by vertical solid brown lines in Figs. 4, 5, and 6 while frequencies of LO modes with A_u symmetry are indicated by vertical dotted brown lines in Figs. 4, 5, and 8.

Mode frequencies identified by Höfer *et al.* are also included in Table VI for comparison, where modes 3, 7, 10, 11, 13, 17, 22, and 23 remained unresolved.

3. TO-LO rule

The TO-LO rule can best be inspected within the BUL form in Eq. (6). If a switch occurs within a set of ascending frequencies $\omega_{\mathrm{TO},l} < \omega_{\mathrm{LO},l} < \omega_{\mathrm{TO},l+1} < \omega_{\mathrm{LO},l+1} \ldots$, for example, $\omega_{\mathrm{TO},l} < \omega_{\mathrm{TO},l+1} < \omega_{\mathrm{LO},l} < \omega_{\mathrm{LO},l+1} \ldots$, then the BUL form produces negative imaginary parts in the spectral region between $\omega_{\mathrm{TO},l+1} \ldots \omega_{\mathrm{LO},l}$. This is obviously unphysical for a dielectric function, which can be measured along a

TABLE VI. Same as for Table V but for phonon mode parameters with A_u symmetry.

Mode	ω_{TO} (cm^{-1})	ω_{LO} (cm^{-1})	γ_{TO} (cm^{-1})	γ_{LO} (cm^{-1})	A_{TO} (cm^{-1})	Γ_{TO} (cm^{-1})	A_{LO} (cm^{-1})	Γ_{LO} (cm^{-1})	$\bar{v}_j$ (Ref. [26])
1	960.0(6)	988.5(0)	6.(4)	9.5(0)	9(4)	−1.(2)	238.(1)	−0.(5)	960.6
2	914.2(8)	956.(7)	5.8(4)	5.(9)	43(3)	−8.(9)	5(7)	−0.(1)	914.4
3	887.1(6)[b]	897.5(4)[b]	7.8(9)[b]	4.9(2)[b]	30(9)[b]	9.(9)[b]	38.9(4)[b]	0.18(4)[b]	
4	883.1(6)[b]	884.8(8)[b]	5.6(0)[b]	6.5(6)[b]	28(4)[b]	−0.(1)[b]	8.0(4)[b]	−0.05(5)[b]	884.9
5	593.(9)	620.5(0)	7.(7)	14.2(5)	22(6)	−1(0)	121.(8)	−1.(6)	592.8
6	560.(1)	570.(8)	12.(4)	12.(6)	18(9)	−1(6)	5(1)	1.(3)	561.1
7	54(6)	54(8)	1(8)	1(3)	1(2)0	1(7)	1(2)	0.(9)	
8	515.(0)	516.(8)	6.(8)	6.(4)	6(6)	1.(9)	2(2)	0.(0)	510.9
9	439.8(4)	473.6(5)	7.(9)	13.3(2)	214.(6)	−13.(1)	10(7)	−1.(3)	437.1
10	411.(9)	412.(6)	2(8)	2(7)	3(9)	−2.(4)	(7)	1.(6)	
11	40(3)	410.0(1)	1(5)	6.(9)	1(6)	−0.(1)	72.(6)	0.(8)	
12	349.6(5)	40(3)	8.2(2)	1(4)	38(2)	1(2)	10[a]	−(2)	345.0
13	339.(5)	341.(7)	7.(1)	8.(1)	19(8)	−2(4)	6.(8)	−0.3(1)	
14	309.9(2)	317.1(0)	6.(6)	5.(7)	20(8)	(6)	19.(3)	0.0(7)	308.8
15	270.(1)	277.7(8)	3.(6)	3.(9)	9(0)	−(3)	29.(4)	0.0(5)	269.9
16	250.5(2)	266.(6)	3.8(2)	2.(7)	29(4)	(9)	16.(0)	−0.0(7)	248.8
17	225.(3)	229.5(3)	3.(7)	2.(3)	1(1)0	(2)0	12.(2)	0.0(1)	
18	223.(5)	224.(3)	3.(7)	2.(3)	1(2)0	−(1)0	2.(2)	−0.0(2)	223.3
19	201.6(2)	207.(0)	3.4(5)	3.(1)	12(3)	1(0)	14.(1)	−0.0(4)	200.9
20	188.8(3)	196.6(8)	2.3(2)	3.(8)	249.(4)	−2(0)	9.5(2)	−0.04(2)	188.5
21	154.(1)[b]	154.(5)[b]	2[a]	2[a]	4(3)[b]	(9)[b]	(3)[b]	0.0(6)[b]	169.9
22	114.(2)	115.(0)	2.(1)	2.(5)	4(3)	−(3)	3.(5)	−0.0(2)	
23	70[a]	73[a]	5[a]	2[a]	4(6)[b]	0.(8)[b]	(3)[b]	0.0(6)[b]	

[a]Manually set parameter held constant throughout fitting procedure.
[b]Parameter fit in a local region, held constant in full spectral fit procedure.

certain, fixed coordinate direction. However, the determinant function in a low-symmetry material does not represent a directly measurable quantity. Rather, it serves as a spectral indicator for the frequencies of TO and LO modes, as shown in this paper. Furthermore, and accordingly, the determinant produces negative imaginary parts when the order of TO and LO modes within the monoclinic plane is such that the TO-LO rule is broken—specifically, between B_u modes 17 → 16, 14 → 13, 11 → 10, 8 → 7, 7 → 6, 6 → 5, 4 → 3, and 2 → 1. Previously we have observed this TO-LO rule broken for monoclinic β-Ga_2O_3 [29] but not for monoclinic $CdWO_4$ [33]. In these cases, when a second TO mode is observed before the next subsequent LO mode, the imaginary part of the determinant is observed to go negative and the imaginary part of the inverse determinant is observed to go positive. Note that the TO-LO rule holds true for all A_u modes.

4. High-frequency and static dielectric constant

Static and high-frequency dielectric constants obtained in this work are summarized in Table VII. Static dielectric constants ε_{DC} for each tensor element were extrapolated from the model calculation at $\omega = 0$, and the high-frequency dielectric constant was an offset parameter in the best-match model analysis. From these, it is determined that the generalized LST relation described by Schubert in Ref. [30] is well satisfied.

TABLE VII. Best-match model parameters for high-frequency dielectric constants along with static dielectric constants extrapolated from the model to $\omega = 0$ for each tensor element.

	ε_{xx}	ε_{yy}	ε_{xy}	ε_{zz}
ε_∞	3.16(6)	3.12(7)	0.002(7)	3.11(4)
ε_{DC}	10.96(5)	9.80(1)	0.12(5)	11.47(4)
$\varepsilon_{\infty,DFT}$	3.570	3.549	−0.041	3.650

V. CONCLUSIONS

The frequency dependence of four independent Cartesian tensor elements of the dielectric function for Y_2SiO_5 were determined using generalized spectroscopic ellipsometry with a dielectric function tensor model approach from 40–1200 cm^{-1}. Three different surfaces cut perpendicular to a principle axis were investigated. We match the spectral dependence of the four wavelength-by-wavelength determined dielectric function tensor elements as well as the four inverse tensor elements along with the determinant and its inverse to those rendered by our monoclinic model in order to determine the 22 pairs of transverse and longitudinal optical phonon modes with B_u symmetry and 23 pairs with A_u symmetry. We make use of two independent sets of anharmonic oscillators to describe TO and LO mode parameters and their eigendielectric displacement vectors within the **a**-**c** plane. We report and compare our experimental findings to density functional theory calculations. We discuss the observation of the violation of the TO-LO rule for polarization within the monoclinic plane. We report the static and high-frequency dielectric tensor constants and find that the generalized Lyddane-Sachs-Teller relation is well satisfied for Y_2SiO_5.

ACKNOWLEDGMENTS

The authors thank Larry Alegria (Scientific Materials Corp.) for detailed information on the samples. This work was supported in part by the National Science Foundation (NSF) through the Center for Nanohybrid Functional Materials (EPS-1004094), the Nebraska Materials Research Science and Engineering Center (MRSEC) (DMR-1420645), and awards CMMI 1337856 and EAR 1521428. The authors further acknowledge financial support by the University of Nebraska-Lincoln, the J. A. Woollam Co., Inc., and the J. A. Woollam Foundation. The DFT calculations were performed using the computing resources of the Holland Computing Center and the Center for Nanohybrid Functional Materials at the University of Nebraska-Lincoln.

[1] C. Li, C. Wyon, and R. Moncorge, IEEE J. Quantum Electron. **28**, 1209 (1992).
[2] P. Sellin, N. Strickland, J. Carlsten, and R. Cone, Opt. Lett. **24**, 1038 (1999).
[3] M. J. Thorpe, L. Rippe, T. M. Fortier, M. S. Kirchner, and T. Rosenband, Nat. Photonics **5**, 688 (2011).
[4] C. W. Thiel, R. L. Cone, and T. Böttger, J. Lumin. **152**, 84 (2014).
[5] Y. Wang, C. Liu, J. Liu, L. Zheng, L. Su, and J. Xu, Opt. Quantum Electron. **47**, 2525 (2015).
[6] S. Cook, T. Rosenband, and D. R. Leibrandt, Phys. Rev. Lett. **114**, 253902 (2015).
[7] W. R. Babbitt, Z. W. Barber, S. H. Bekker, M. D. Chase, C. Harrington, K. D. Merkel, R. K. Mohan, T. Sharpe, C. R. Stiffler, A. S. Traxinger *et al.*, Laser Phys. **24**, 094002 (2014).
[8] E. Saglamyurek, N. Sinclair, J. A. Slater, K. Heshami, D. Oblak, and W. Tittel, New J. Phys. **16**, 065019 (2014).
[9] A. I. Lvovsky, B. C. Sanders, and W. Tittel, Nat. Photonics **3**, 706 (2009).
[10] N. Sangouard, C. Simon, H. De Riedmatten, and N. Gisin, Rev. Mod. Phys. **83**, 33 (2011).
[11] F. Bussières, N. Sangouard, M. Afzelius, H. de Riedmatten, C. Simon, and W. Tittel, J. Mod. Opt. **60**, 1519 (2013).
[12] C. Thiel, T. Böttger, and R. Cone, J. Lumin. **131**, 353 (2011).
[13] A. V. Turukhin, V. S. Sudarshanam, M. S. Shahriar, J. A. Musser, B. S. Ham, and P. R. Hemmer, Phys. Rev. Lett. **88**, 023602 (2001).
[14] B. Sengthong, P. Van Do, J. W. Chung, G. A. Kumar, V. X. Quang, V.-D. Dao, Y.-I. Lee *et al.*, RSC Adv. **6**, 92454 (2016).
[15] S. H. Shin, D. Y. Jeon, and K. S. Suh, Jpn. J. Appl. Phys. **40**, 4715 (2001).
[16] A. Meijerink, W. Schipper, and G. Blasse, J. Phys. D **24**, 997 (1991).
[17] P. Born, D. Robertson, and P. Smith, J. Mater. Sci. Lett. **4**, 497 (1985).
[18] A. G. De Mesquita and A. Bril, J. Electrochem. Soc. **116**, 871 (1969).
[19] M. Nikl, A. Vedda, and V. V. Laguta, in *Springer Handbook of Crystal Growth*, edited by G. Dhanaraj, K. Byrappa, V. Prasad, and M. Dudley (Springer, Berlin, Heidelberg, 2010), pp. 1663–1700.
[20] Z. Li, J. Liu, P. Yu, and G. Zhang, Appl. Phys. B **122**, 109 (2016).
[21] Y.-K. Kuo, M.-F. Huang, and M. Birnbaum, IEEE J. Quantum Electron. **31**, 657 (1995).
[22] C. Deka, B. Chai, Y. Shimony, X. Zhang, E. Munin, and M. Bass, Appl. Phys. Lett. **61**, 2141 (1992).
[23] A. N. Lazarev, T. F. Tenisheva, I. A. Bondar', and N. A. Toropov, Bull. Acad. Sci. USSR **12**, 1115 (1963).
[24] Y. K. Voron'ko, A. A. Sobol, V. E. Shukshin, A. I. Zagumennyi, Y. D. Zavartsev, and S. A. Koutovoi, Opt. Mater. **33**, 1331 (2011).
[25] L. Zheng, G. Zhao, C. Yan, X. Xu, L. Su, Y. Dong, and J. Xu, J. Raman Spectrosc. **38**, 1421 (2007).
[26] S. Höfer, R. Uecker, A. Kwasniewski, J. Popp, and T. G. Mayerhöfer, Vib. Spectrosc. **83**, 151 (2016).
[27] H. Fujiwara, *Spectroscopic Ellipsometry Principals and Applications* (Maruzen Co. Ltd., Tokyo, 2003).
[28] G. E. Jellison, Jr., E. D. Specht, L. A. Boatner, D. J. Singh, and C. L. Melcher, J. Appl. Phys. **112**, 063524 (2012).
[29] M. Schubert, R. Korlacki, S. Knight, T. Hofmann, S. Schöche, V. Darakchieva, E. Janzén, B. Monemar, D. Gogova, Q.-T. Thieu *et al.*, Phys. Rev. B **93**, 125209 (2016).
[30] M. Schubert, Phys Rev. Lett. **117**, 215502 (2016).
[31] M. Born and K. Huang, *Dynamical Theory of Crystal Lattices* (Clarendon Press, Oxford, 1954).
[32] A. Mock, R. Korlacki, C. Briley, V. Darakchieva, B. Monemar, Y. Kumagai, K. Goto, M. Higashiwaki, and M. Schubert, Phys. Rev. B **96**, 245205 (2017).
[33] A. Mock, R. Korlacki, S. Knight, and M. Schubert, Phys. Rev. B **95**, 165202 (2017).
[34] R. H. Lyddane, R. Sachs, and E. Teller, Phys. Rev. **59**, 673 (1941).
[35] D. W. Berreman and F. C. Unterwald, Phys. Rev. **174**, 791 (1968).
[36] R. P. Lowndes, Phys. Rev. B **1**, 2754 (1970).
[37] B. Liu, J. Wang, F. Li, L. Sun, J. Wang, and Y. Zhou, J. Am. Ceram. Soc. **96**, 3304 (2013).
[38] Y. Luo, J. Wang, J. Wang, J. Li, and Z. Hu, J. Am. Ceram. Soc. **97**, 945 (2014).
[39] W. Y. Ching, L. Ouyang, and Y.-N. Xu, Phys. Rev. B **67**, 245108 (2003).
[40] J. Felsche, in *Rare Earths*, Vol. 13 (Springer, 1973), pp. 99–197.
[41] T. Hahn, editor, *International Tables for Crystallography* (Kluwer Academic Publishers, Dordrecht, 1992), Vol. A.
[42] O. Kennard, J. C. Speakman, and J. D. H. Donnay, Acta Cryst. **22**, 445 (1967).
[43] A. D. Mighell, J. Res. Natl. Inst. Stand. Technol. **107**, 373 (2002).
[44] L. A. Harris and C. B. Finch, Amer. Miner. **50**, 1493 (1965).
[45] C. Michel, G. Buisson, and E. F. Bertaut, Comptes Rendus Acad. Sci. **264**, 397 (1967).
[46] B. A. Maksimov, Y. A. Kharitonov, V. V. Ilyukhin, and N. V. Belov, Dokl. Acad. Nauk SSSR **183**, 1072 (1968) [Sov. Phys. Dokl. **13**, 1188 (1969)].
[47] N. Leonyuk, E. Belokoneva, G. Bocelli, L. Righi, E. Shvanskii, R. Henrykhson, N. Kulman, and D. Kozhbakhteeva, J. Cryst. Growth **205**, 361 (1999).
[48] Quantum ESPRESSO is available from http://www.quantum-espresso.org. See also: P. Giannozzi, S. Baroni, N. Bonini, M. Calandra, R. Car, C. Cavazzoni, D. Ceresoli, G. L. Chiarotti,

M. Cococcioni, I. Dabo, A. D. Corso, S. de Gironcoli, S. Fabris, G. Fratesi, R. Gebauer, U. Gerstmann, C. Gougoussis, A. Kokalj, M. Lazzeri, L. Martin-Samos, N. Marzari, F. Mauri, R. Mazzarello, S. Paolini, A. Pasquarello, L. Paulatto, C. Sbraccia, S. Scandolo, G. Sclauzero, A. P. Seitsonen, A. Smogunov, P. Umari, and R. M. Wentzcovitch, J. Phys.: Condens. Matter **21**, 395502 (2009).

[49] J. P. Perdew and A. Zunger, Phys. Rev. B **23**, 5048 (1981).

[50] D. R. Hamann, Phys. Rev. B **88**, 085117 (2013).

[51] Code available from http://www.mat-simresearch.com.

[52] M. Schlipf and F. Gygi, Comput. Phys. Commun. **196**, 36 (2015).

[53] K. Momma and F. Izumi, J. Appl. Cryst. **44**, 1272 (2011).

[54] T. Björkman, Comput. Phys. Commun. **182**, 1183 (2011).

[55] H. J. Monkhorst and J. D. Pack, Phys. Rev. B **13**, 5188 (1976).

[56] F. Gervais and B. Piriou, J. Phys. C: Solid State Phys. **7**, 2374 (1974).

[57] S. Schöche, T. Hofmann, R. Korlacki, T. E. Tiwald, and M. Schubert, J. Appl. Phys. **113**, 164102 (2013).

[58] M. Schubert, T. E. Tiwald, and C. M. Herzinger, Phys. Rev. B **61**, 8187 (2000).

[59] M. Schubert, T. Hofmann, C. M. Herzinger, and W. Dollase, Thin Solid Films **455**, 619 (2004).

[60] T. G. Mayerhöfer, V. Ivanovski, and J. Popp, Spectrochim. Acta, Part A **168**, 212 (2016).

[61] M. Dressel, B. Gompf, D. Faltermeier, A. K. Tripathi, J. Pflaum, and M. Schubert, Opt. Exp. **16**, 19770 (2008).

[62] M. Schubert, C. Bundesmann, G. Jakopic, and H. Arwin, Appl. Phys. Lett. **84**, 200 (2004).

[63] N. Ashkenov, B. N. Mbenkum, C. Bundesmann, V. Riede, M. Lorenz, E. M. Kaidashev, A. Kasic, M. Schubert, M. Grundmann, G. Wagner, and H. Neumann, J. Appl. Phys. **93**, 126 (2003).

[64] A. Kasic, M. Schubert, S. Einfeldt, D. Hommel, and T. E. Tiwald, Phys. Rev. B **62**, 7365 (2000).

[65] A. Kasic, M. Schubert, Y. Saito, Y. Nanishi, and G. Wagner, Phys. Rev. B **65**, 115206 (2002).

[66] V. Darakchieva, P. P. Paskov, E. Valcheva, T. Paskova, B. Monemar, M. Schubert, H. Lu, and W. J. Schaff, Appl. Phys. Lett. **84**, 3636 (2004).

[67] V. Darakchieva, J. Birch, M. Schubert, T. Paskova, S. Tungasmita, G. Wagner, A. Kasic, and B. Monemar, Phys. Rev. B **70**, 045411 (2004).

[68] V. Darakchieva, E. Valcheva, P. P. Paskov, M. Schubert, T. Paskova, B. Monemar, H. Amano, and I. Akasaki, Phys. Rev. B **71**, 115329 (2005).

[69] V. Darakchieva, T. Paskova, M. Schubert, H. Arwin, P. P. Paskov, B. Monemar, D. Hommel, M. Heuken, J. Off, F. Scholz, B. A. Haskell, P. T. Fini, J. S. Speck, and S. Nakamura, Phys. Rev. B **75**, 195217 (2007).

[70] V. Darakchieva, M. Schubert, T. Hofmann, B. Monemar, Y. Takagi, and Y. Nanishi, Appl. Phys. Lett. **95**, 202103 (2009).

[71] V. Darakchieva, T. Hofmann, M. Schubert, B. E. Sernelius, B. Monemar, P. O. A. Persson, F. Giuliani, E. Alves, H. Lu, and W. J. Schaff, Appl. Phys. Lett. **94**, 022109 (2009).

[72] V. Darakchieva, K. Lorenz, N. Barradas, E. Alves, B. Monemar, M. Schubert, N. Franco, C. Hsiao, L. Chen, W. Schaff, L. Tu, T. Yamaguchi, and Y. Nanishi, Appl. Phys. Lett. **96**, 081907 (2010).

[73] M.-Y. Xie, M. Schubert, J. Lu, P. O. A. Persson, V. Stanishev, C. L. Hsiao, L. C. Chen, W. J. Schaff, and V. Darakchieva, Phys. Rev. B **90**, 195306 (2014).

[74] M.-Y. Xie, N. B. Sedrine, S. Schöche, T. Hofmann, M. Schubert, L. Hong, B. Monemar, X. Wang, A. Yoshikawa, K. Wang, T. Araki, Y. Nanishi, and V. Darakchieva, J. Appl. Phys. **115**, 163504 (2014).

[75] T. Hofmann, D. Schmidt, and M. Schubert, in *Ellipsometry at the Nanoscale* (Springer, Berlin, 2013), THz generalized ellipsometry characterization of highly-ordered 3-dimensional nanostructures, pp. 411–428.

[76] D. Sekora, C. Briley, M. Schubert, and E. Schubert, Appl. Surf. Sci. **421**, 783 (2017).

[77] A. Mock, T. Carlson, J. VanDerslice, J. Mohrmann, J. A. Woollam, E. Schubert, and M. Schubert, Appl. Surf. Sci. **421**, 663 (2017).

[78] G. E. Jellison, M. A. McGuire, L. A. Boatner, J. D. Budai, E. D. Specht, and D. J. Singh, Phys. Rev. B **84**, 195439 (2011).

[79] C. Sturm, J. Furthmüller, F. Bechstedt, R. Schmidt-Grund, and M. Grundmann, APL Mater. **3**, 106106 (2015).

[80] C. Sturm, R. Schmidt-Grund, C. Kranert, J. Furthmüller, F. Bechstedt, and M. Grundmann, Phys. Rev. B **94**, 035148 (2016).

[81] C. Sturm, R. Schmidt-Grund, V. Zviagin, and M. Grundmann, Appl. Phys. Lett. **111**, 082102 (2017).

[82] H. Fujiwara, *Spectroscopic Ellipsometry: Principles and Applications* (John Wiley & Sons, Chichester West Sussex, England, 2007).

[83] M. Schubert, Phys. Rev. B **53**, 4265 (1996).

[84] M. Schubert, in *Introduction to Complex Mediums for Optics and Electromagnetics*, edited by W. S. Weiglhofer and A. Lakhtakia (SPIE, Bellingham, WA, 2004), pp. 677–710.

[85] M. Schubert, *Infrared Ellipsometry on Semiconductor Layer Structures: Phonons, Plasmons, and Polaritons*, Springer Tracts in Modern Physics, (Springer, Berlin, 2004), Vol. 209.

[86] M. Schubert, in *Handbook of Ellipsometry*, edited by E. Irene and H. Tompkins (William Andrew Publishing, Norwich, 2004).

[87] C. Traum, P. Inácio, C. Felix, P. Segonds, A. Pena, J. Debray, B. Boulanger, Y. Petit, D. Rytz, G. Montemezzani *et al.*, Opt. Mater. Express **4**, 57 (2014).

[88] M. Schubert, in *Introduction to Complex Mediums for Optics and Electromagnetics*, edited by W. S. Weiglhofer and A. Lakhtakia (SPIE, Bellingham, WA, 2003).

[89] M. Schubert, Ann. Phys. **15**, 480 (2006).

[90] S. Baroni, S. de Gironcoli, A. D. Corso, S. Baroni, S. de Gironcoli, and P. Giannozzi, Rev. Mod. Phys. **73**, 515 (2001).

[91] A. Kokalj, Comput. Mater. Sci. **28**, 155 (2003). Code available from http://www.xcrysden.org.